

REPORT DOCUMENTATION PAGE

Form Approved  
OME No. 0704-0188

AD-A264 827



Information is estimated to average 1 hour per message and using the limits for handling instructions, including printing, sorting, copying and reviewing the distribution of information. The comments regarding this burden estimate or any other aspect of this including this burden to Washington Headquarters Services, Directorate for Information Operations and Reports, 1215 Jefferson Ave, and to the Office of Management and Budget, Paperwork Reduction Project (0704-0188), Washington, DC 20503.

2. REPORT DATE  
1993, March 1

3. REPORT TYPE AND DATES COVERED  
Annual  
2/1/92-1/31/93

4. TITLE AND SUBTITLE  
(U) Detailed Studies of Soot Formation in Laminar Diffusion Flames for Application to Modeling Studies

5. FUNDING NUMBERS  
PE - 61102F  
PR - 2308  
SA - BS  
G - F49620-92-D-0161

6. AUTHOR(S)  
Robert J. Santoro

7. PERFORMING ORGANIZATION NAME(S) AND ADDRESS(ES)  
The Pennsylvania State University  
Department of Mechanical Engineering  
University Park, PA 16802

8. PERFORMING ORGANIZATION REPORT NUMBER

9. SPONSORING/MONITORING AGENCY NAME(S) AND ADDRESS(ES)  
AFOSR/NA  
110 Duncan Avenue, Suite B115  
Bolling AFB, DC 20332-0001

10. SPONSORING/MONITORING AGENCY REPORT NUMBER

DTIC  
S ELECTE D  
MAY 14 1993  
C

11. SUPPLEMENTARY NOTES

12. DISTRIBUTION/AVAILABILITY STATEMENT

Approved for public release; distribution is unlimited

93-10650



53 pp

~~93 5 12 10 8~~

A study of soot particle formation in laminar diffusion flames has been undertaken to investigate soot precursor chemistry, particle inception and surface growth phenomena. During the first year of this study emphasis has been given to species concentrations measurements made using mass spectrometric techniques. These measurements have demonstrated that species measurements can be obtained in particle laden regions of diffusion flames using a novel sampling probe approach. In particular, measurements have been obtained of acetylene, diacetylene, benzene and stable combustion products throughout methane/air and ethene/air laminar diffusion flames. Combining these measurements with previous soot particle and velocity field measurements it has been possible to follow the soot growth process along individual particle paths. These results establish that soot particle growth ceases due to the depletion of growth species not through the loss of soot particle reactivity as observed in premixed flame studies.

Similarly, laser-induced fluorescence measurements of polynuclear aromatic hydrocarbons have been undertaken to follow the evolution of the soot precursor field. These measurements have established that laser-induced fluorescence can be used to reveal the qualitative structure of the molecular growth process leading to soot particle formation. These results need to be extended to provide more quantitative comparisons, particularly regarding fuel structure effect.

Additional studies have been carried out to characterize the effects of aggregates on the interpretation of light scattering measurements. The results of these studies have shown that through the incorporation of fractal analysis a self-consistent treatment of aggregates can be incorporated into the light scattering analysis.

14. SUBJECT TERMS  
Soot Formation, Soot Particles, Diffusion Flames

15. NUMBER OF PAGES  
50

16. PRICE CODE

17. SECURITY CLASSIFICATION OF REPORT  
Unclassified

18. SECURITY CLASSIFICATION OF THIS PAGE  
Unclassified

19. SECURITY CLASSIFICATION OF ABSTRACT  
Unclassified

20. LIMITATION OF ABSTRACT  
UL

Annual Report  
on  
Detailed Studies of Soot Formation in Laminar Diffusion Flames  
for Application to Modeling Studies

AFOSR Grant F49620-92-J-0161

Prepared by

Robert J. Santoro  
Department of Mechanical Engineering  
The Pennsylvania State University  
University Park, PA 16802

Submitted to

Air Force Office of Scientific Research  
Bolling Air Force Base  
Washington, DC

DTIC QUALITY INSPECTED 5

March 1993

Accession For	
NTIS CRA&I	<input checked="" type="checkbox"/>
DTIC TAB	<input type="checkbox"/>
Unannounced	<input type="checkbox"/>
Justification _____	
By _____	
Distribution/	
Availability Codes	
Dist	Avail and/or Special
A-1	

## Table of Contents

	<u>Page</u>
Cover Page . . . . .	i
Table of Contents . . . . .	iii
Summary . . . . .	iv
1.0 Research Objectives . . . . .	1
2.0 Research Approach . . . . .	2
2.1 Pulse-Dye Laser Fluorescence System . . . . .	3
2.2 Intrusive Probe Sampling for Species Concentration Measurements . . . . .	4
3.0 Research Accomplishments . . . . .	8
3.1 Species Concentration Measurements . . . . .	8
3.2 Laser-Induced Fluorescence Measurements of PAH Species . . . . .	19
3.3 Aerosol Dynamic Processes of Soot Aggregates in Diffusion Flames . . . . .	28
4.0 Conclusions . . . . .	29
5.0 References . . . . .	30
6.0 Publications . . . . .	32
7.0 Meetings and Presentations . . . . .	32
8.0 Participating Professions . . . . .	32
9.0 Interactions . . . . .	33
Appendix A. Aerosol Dynamic Processes of Soot Aggregates in a Laminar Ethene Diffusion Flame	34

## Summary

A study of soot particle formation in laminar diffusion flames has been undertaken to investigate soot precursor chemistry, particle inception and surface growth phenomena. During the first year of this study emphasis has been given to species concentrations measurements made using mass spectrometric techniques. These measurements have demonstrated that species measurements can be obtained in particle laden regions of diffusion flames using a novel sampling probe approach. In particular, measurements have been obtained of acetylene, diacetylene, benzene and stable combustion products throughout methane/air and ethene/air laminar diffusion flames. Combining these measurements with previous soot particle and velocity field measurements it has been possible to follow the soot growth process along individual particle paths. These results establish that soot particle growth ceases due to the depletion of growth species not through the loss of soot particle reactivity as observed in premixed flame studies.

Similarly, laser-induced fluorescence measurements of polynuclear aromatic hydrocarbons have been undertaken to follow the evolution of the soot precursor field. These measurements have established that laser-induced fluorescence can be used to reveal the qualitative structure of the molecular growth process leading to soot particle formation. These results need to be extended to provide more quantitative comparisons, particularly regarding fuel structure effect.

Additional studies have been carried out to characterize the effects of aggregates on the interpretation of light scattering measurements. The results of these studies have shown that through the incorporation of fractal analysis a self-consistent treatment of aggregates can be incorporated into the light scattering analysis.

## 1.0 Research Objectives

The objective of this research effort is to investigate the fundamental phenomena controlling soot particle formation and destruction in combustion systems. The emphasis and approach chosen for the present studies is based on previous results developed under AFOSR support which have proven the soundness of the methodology being utilized [1-10]. The present studies are conducted in a series of well-characterized laminar diffusion flames in which fuel constituents, temperature, concentration and transport processes are systematically varied and/or measured. A laminar diffusion flame environment has been selected because it provides a relatively simple environment in which mixing processes are important while allowing for a wide range of measurement techniques to be employed. The importance of mixing in practical combustor situations is well recognized and, thus, it is critical to study soot formation processes under conditions where mixing has a significant role.

Specifically, the current effort emphasizes detailed measurements of the preparticle chemistry, particle inception and surface growth phenomena important in soot particle formation. These studies are intended to yield quantitative measurements of the precursor and surface growth species which contribute to soot particle formation and growth. Data, which is temporally and spatially resolved, are of great value to modeling studies as past studies have demonstrated [11-14]. In fact, the availability of such results has allowed significant progress to be achieved over the past decade in soot modeling capabilities. In particular, current modeling studies being conducted by Prof. M. Frenklach at Penn State will be very beneficial in terms of providing comparisons with the present measurements.

During the first year of this study efforts have emphasized measurements of species concentration, especially acetylene and benzene concentrations, throughout the flame using a mass spectrometric approach. Additionally, laser-induced fluorescence measurements have been obtained to characterize the evolution of large polynuclear aromatic species (PAH) formed in the flame. These

measurements are being combined with previous determinations of the soot particle, velocity and temperature fields to yield more detailed information on the soot growth process.

## 2.0 Research Approach

For the present studies, a coannular laminar diffusion flame has been selected for study. This flame configuration has been widely studied recently and has been the focus of extensive fuel molecular structure and pressure sensitivity studies in our laboratory [1-10]. Since practical combustors typically involve the separate injection of fuel and oxidizer, laminar diffusion flames provide a simple, tractable environment in which to study soot formation while maintaining conditions where mixing effects are important. Soot formation can be viewed as a series of sequential processes which occur to some degree in all combustion environments where soot is observed. It is the relative importance of these processes and their coupling which determines the amount of soot formed, its distribution throughout the combustion zone and its eventual emission from a specific combustor. Essential to the study of these processes is the selection of an experimental configuration which can provide the range of conditions typical of fuel-rich combustion zones. Laminar coannular diffusion flame studies have clearly demonstrated that such conditions can be achieved and studied [5]. Furthermore, such studies are proving to be increasingly valuable for the validation of modeling studies. With these points in mind, the coannular laminar diffusion flame represents a highly attractive experimental configuration for the present studies.

The studies during the current year have been conducted in an atmospheric diffusion flame facility consisting of a coannular diffusion flame burner, burner chimney, positioning system and gas metering system. The burner has a configuration consisting of a 1.1 cm fuel tube surrounded by a 10 cm air annulus. The air passage is partially filled with glass beads followed by a series of fine screens to provide flow conditioning. A ceramic honeycomb 2.54 cm in thickness is used at the exit to provide a uniform flow field. The fuel tube which extends 4.8 mm above the ceramic honeycomb also is partly filled with glass beads to condition the flow. The fuel flow can consist of up to three

gases, each metered with a separate rotameter. This allows for mixtures of fuels as well as nitrogen dilution of the fuel for temperature and concentration variation. The air flow is metered using a mass flowmeter which can monitor flows up to 5 SCFM of air. To protect the flame from room disturbances, a metal chimney has been incorporated into the burner facility. The chimney translates horizontally with the burner while sliding vertically within the chimney. Slots machined in the chimney provide access for the optical and intrusive probing of the flame.

The burner is mounted on a pair of motorized translating stages which provide for vertical and horizontal motion. A manual translation stage is also included to allow for adjustment in the second horizontal direction and is used to align the burner with the laser scattering system. The motorized stages are used to traverse the burner through the laser beam to obtain measurements over the cross section of the flame at a particular height in the flame.

A variety of diagnostic techniques are available for application to these studies to measure the soot particle, temperature, species concentration and velocity fields. Both non-intrusive laser-based techniques, such as laser light scattering, laser velocimetry and laser-induced fluorescence, and intrusive probing followed by mass spectrometric and gas chromatographic analysis are utilized in these studies. During the past year, measurements employing laser-induced fluorescence and mass spectrometry have been emphasized. A brief description of the apparatus used for these measurements follows for the reader's information.

### **2.1 Pulse-Dye Laser Fluorescence System**

An Nd-Yag pulsed-dye laser system is utilized for fluorescence detection of OH radicals as well as for PAH species measurements. The major components of the system involve the dye laser, which consists of an Nd-Yag pulsed laser operating at 532 nm, a dye laser module and a doubling crystal. The present system has the capability to tune over a wavelength range extending from 220 to 600 nm. This wavelength range is quite suitable for OH fluorescence as well as PAH measurements. Detection is achieved using a spectrometer-photomultiplier combination or an intensified CCD array

camera. In the case of the photomultiplier, the PMT signal is input to a box car integrator to provide for signal averaging and background noise rejection. For the intensified CCD array camera, direct storage of the images on a personal computer is used to record the data. This unit has a 50 ns gate capability and can be used for signal averaging of multiple laser shots. Using this camera, planar laser imaging is also possible, which allows spatially extensive measurements to be obtained. The OH concentration measurements have previously been obtained throughout similar diffusion flames using this system [10].

## 2.2 Intrusive Probe Sampling for Species Concentration Measurements

In order to provide more quantitative information on the species important in the formation and growth of soot particles, a mass spectrometer system has been assembled for these studies. Gas samples from the flames under study are obtained using a quartz microprobe technique similar to the approach taken by Smyth *et al.* [15]. Measurements of gas phase species in the soot precursor and particle inception regions can be obtained. Measurements in the present studies are also extended into the surface growth region in order to ascertain the important species responsible for mass addition through surface growth. As part of the current research program, approaches allowing sampling of fuel-rich particle laden regions have been developed which allow measurements in the post-particle inception region of the flame. The need to determine gas species concentrations in regions containing soot particles presents serious diagnostic challenges. In general, optical diagnostic techniques can measure only a limited number of species and, in some cases, cannot be reliably applied in the presence of soot particles. Sampling probe techniques usually are limited by orifice clogging problems which can only be overcome by increasing the orifice dimensions at the sacrifice of spatial resolution of the measurements. To overcome the aforementioned orifice clogging problem, a novel sonic sampling probe has been developed and applied to a series of laminar diffusion flames containing various amounts of soot. The details of the design and operation of this probe were recently presented at the Eastern States Meeting of The Combustion Institute [16].

The approach, employed to prevent clogging of the probe orifice, involves mechanically oscillating a wire through the orifice region using a spring-loaded solenoid plunger whose driving circuit is electronically interrupted periodically (see Figure 1). The constant motion of the wire relative to the quartz tube is responsible for keeping the orifice open. For the present probe, the effective orifice is the annulus formed by an oscillating 130  $\mu\text{m}$  diameter Sapphire fiber of uniform cross section and the 160  $\mu\text{m}$  diameter orifice in the quartz tube. Therefore, the effective orifice is equivalent to approximately a 100  $\mu\text{m}$  circular hole. The Sapphire fiber is attached to a 1.59 mm tube which is connected to a spring-loaded soft iron solenoid plunger which oscillates in the orifice. This probe is referred to as the electromechanic sonic probe (EMS) since it employs a sonic sampling orifice with an electromagnetic mechanism to maintain the integrity of the orifice opening.

The mass spectrometer used for these studies utilizes a quadrupole mass filter with a mass range of 1 to 500 amu. This unit (an Extrel Model C-50) has excellent mass resolution (0.1 amu) and high sensitivity. The probe and mass spectrometer assembly are differentially pumped (see Figure 2). A pressure of between 1 and 10 torr using a vacuum roughing pump is achieved directly behind the quartz orifice. Sampling from this low pressure region is provided by a second probe. This second probe is used to introduce gases into the mass spectrometer which is maintained at a pressure near  $10^{-6}$  torr using a turbomolecular pumping system.

Radial profiles of the species concentration as a function of axial position are obtained by transversing the flame in the radial direction. Data acquisition and the control of the mass spectrometer has been implemented using a laboratory personal computer system. This capability allows for rapid and convenient data acquisition, while also affording opportunities for new probing approaches such as rapid insertion sampling. When these measurements are combined with the soot particle and velocity measurements, the temporal evolution of the species concentration and its relationship to soot formation can be investigated.

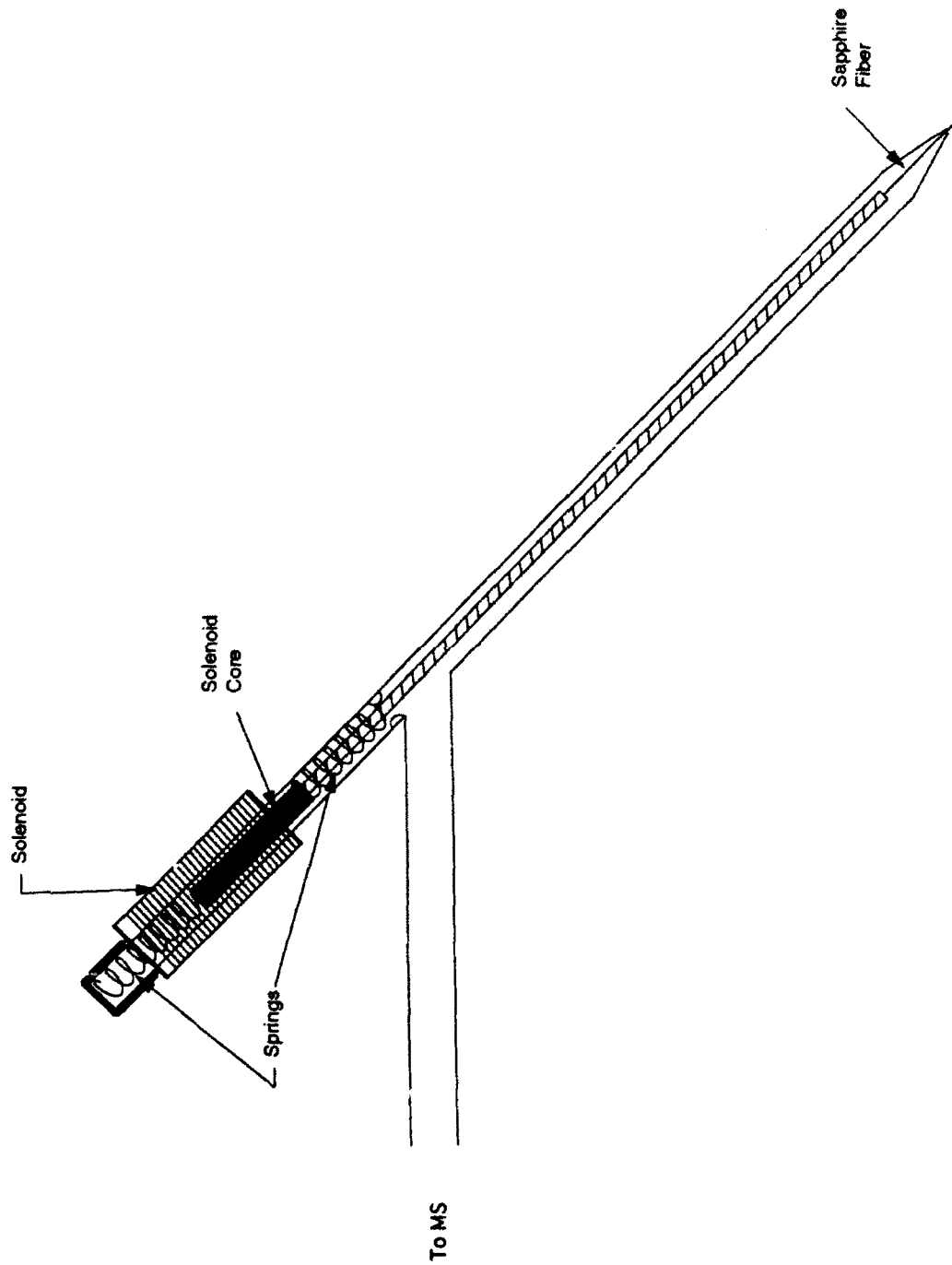


Figure 1. Schematic representation of the electromagnetic sonic probe.

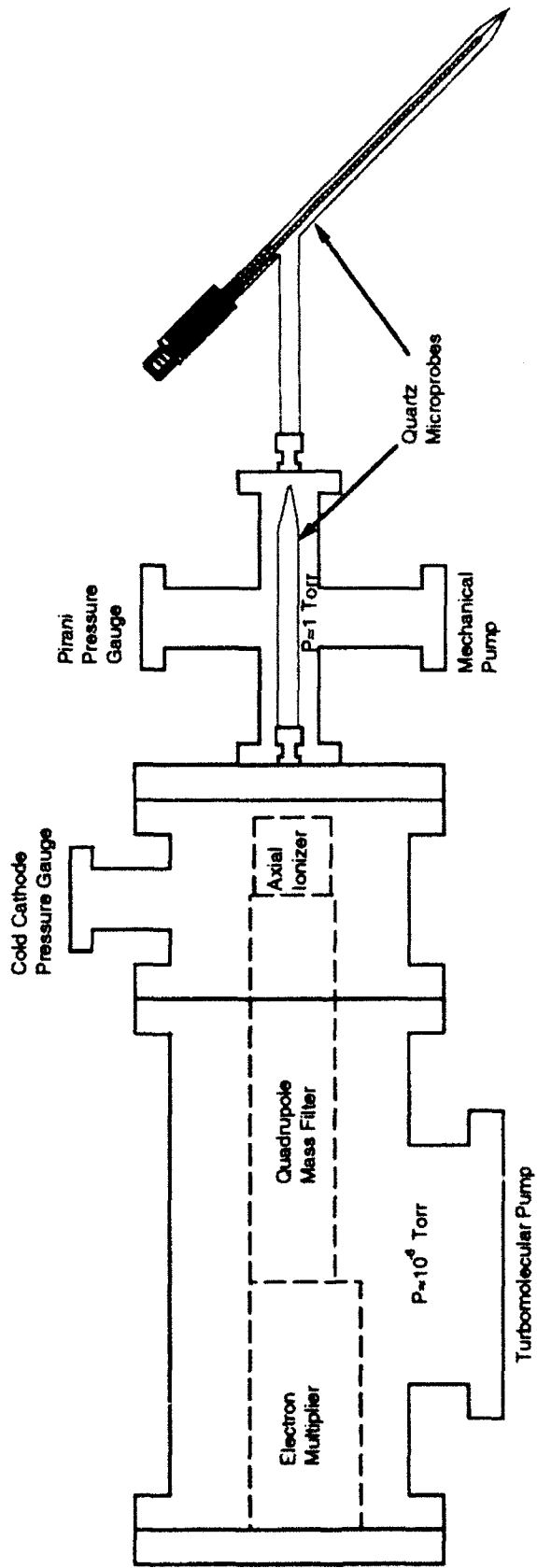


Figure 2. Schematic representation of the quadrupole mass spectrometer and probe assembly.

### 3.0 Research Accomplishments

In the following sections research accomplishments achieved over the first year of the current AFOSR grant are summarized. Specifically, three areas of activities are described:

(1) species concentration measurements, (2) laser-induced fluorescence results for PAH species and (3) light scattering analysis for aggregated soot particles. This last topic is only briefly described since a recent publication has appeared in *Combustion and Flame* which is included as Appendix A.

#### 3.1 Species Concentration Measurements

During the past year detailed species concentration measurements have been obtained in laminar diffusion flames burning methane and ethene fuels in air. These flames have been studied before attempting to investigate fuel mixture flames, which involve a wide range of fuel structures, in order to firmly establish the capabilities of the sampling and species measurement approach. Additionally, both these flames have been previously studied in our laboratory and, thus, the present species concentration measurements significantly enhance that available data base. In particular for the ethene diffusion flame case, a large data base exists on soot volume fraction, number density and particle diameter as well as on temperature, velocity, OH concentrations and PAH fluorescence. The species concentration measurements complement this existing data and allow more sophisticated analysis of the soot formation process for this flame.

##### Methane Flame Results

A methane/air diffusion flame with a fuel flow rate of  $5.7 \text{ cm}^3/\text{s}$  and an air flow of  $1062 \text{ cm}^3/\text{s}$  was selected for study because this flame produces relatively low amounts of soot and has been extensively studied by other workers [17]. Species measurements using gas chromatographic analysis obtained by Mitchell et al. [17] and also by Puri [18] in our laboratory allowed direct comparison with the mass spectrometric analysis used in the present work. The modest soot loading also allowed comparisons between results obtained with the EMS probe and more conventional quartz microprobes. Comparisons with previous results showed good agreement with species having mole

fractions greater than the 0.1 with agreement to within  $\pm 10\%$  while those with mole fractions less than 0.1 agreed to within  $\pm 15\%$ . The exception to these observations was hydrogen ( $H_2$ ) which showed differences as large as  $\pm 50\%$ . This is not surprising since hydrogen is difficult to measure using either gas chromatography or mass spectrometry. The major species considered in the flame were  $N_2$ ,  $O_2$ ,  $CH_4$ ,  $H_2O$ ,  $CO_2$ ,  $H_2$ ,  $C_2H_2$ , and Ar. Preliminary measurements were also obtained for diacetylene ( $C_4H_2$ ) and benzene ( $C_6H_6$ ). However, calibrations for these species have not yet been performed and only relative signal intensities can be presented at this time. It should also be noted that the interference between  $N_2$  and CO at mass 28 amu makes CO difficult to measure. Thus, CO concentration measurements are excluded at present.

Figure 3 shows mole fraction profiles as a function of horizontal position for  $CH_4$ ,  $C_2H_2$  and  $H_2$  in the methane/air diffusion flame for four axial locations. As Figure 3a indicates, the fuel is rapidly consumed as it diffuses to the flame front and by 50 mm above the fuel tube exit has completely disappeared. Of marked interest for the soot formation phenomena are the profiles of  $C_2H_2$  which is generally viewed as the major species involved in soot particle surface growth. Acetylene ( $C_2H_2$ ) shows slightly different features as compared to the  $CH_4$  results (see Figure 3b). Although it is also totally consumed by the 50 mm axial location,  $C_2H_2$  initially appears to be formed away from the center line region as indicated by the local maximums near 10 and 22 mm along the horizontal coordinate. Additionally, the mole fraction of  $C_2H_2$  increases with height until the 24 mm axial location after which it rapidly decreases to zero at the 50 mm axial location. Hydrogen follows a similar trend (see Figure 3c) except appreciable amounts of  $H_2$  are still observed at the 50 mm axial location. Measurements of  $O_2$  show that no  $O_2$  is present at the center line for the 50 mm axial location indicating that the stoichiometric flame tip occurs above this height.

In summary, these methane flame results demonstrate that the present mass spectrometric sampling system can obtain spatially resolved species concentration measurements throughout these diffusion flames. Differences in the evolution of major species can be resolved and relative rates of

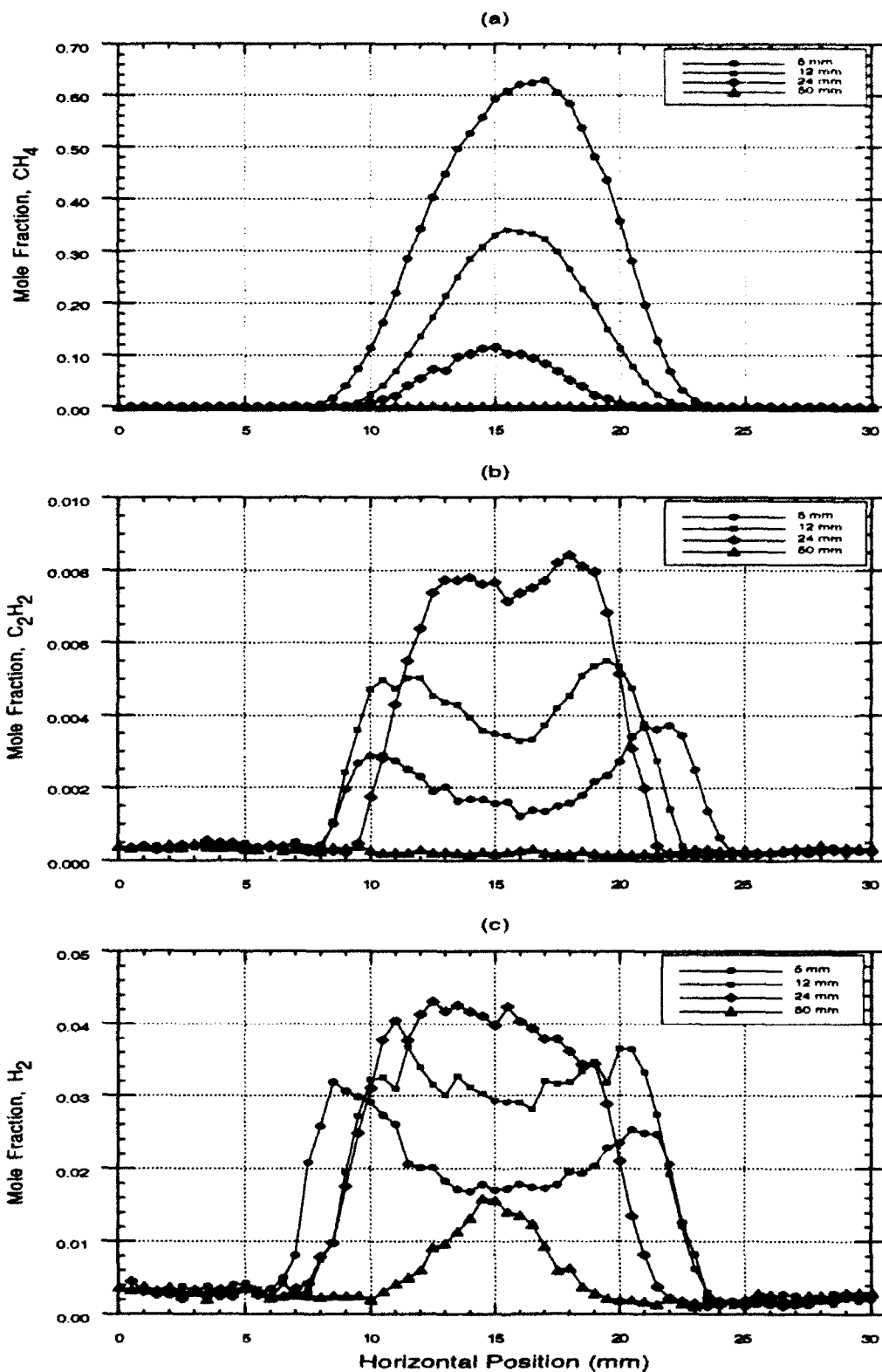


Figure 3.

Plots of the measured species mole fractions as a function of horizontal position for several axial locations (5, 12, 24, and 50 mm) in a CH<sub>4</sub>/Air diffusion flame with a fuel flow rate of 5.7 cm<sup>3</sup>/s: a) CH<sub>4</sub> mole fractions, b) C<sub>2</sub>H<sub>2</sub> mole fractions, c) H<sub>2</sub> mole fractions.

production and destruction can be determined. The present measurements are in good agreement with previous measurements and validate the application of the EMS probe to more heavily sooting flames where no previous measurements exist. Further comparisons with these methane flame results will be discussed after the ethene flame results are described.

### Ethene Flame Results

Similar species concentration measurements were obtained in an ethene/air laminar diffusion flame having a fuel flow rate of  $3.85 \text{ cm}^3/\text{s}$ . Although this flame does not emit soot particles from its tip, the peak soot volume fraction observed in this flame exceeds  $10^{-5}$ . Consequently, the EMS microprobe is essential to achieving measurements in this flame.

Figure 4 shows the measured mole fraction profiles of  $\text{C}_2\text{H}_4$ ,  $\text{C}_2\text{H}_2$  and  $\text{H}_2$  at several axial locations in the ethene/air diffusion flame. The general trends observed for the evolution of fuel concentration are similar to the methane flame results (see Figures 3a and 4a). Additionally, the  $\text{C}_2\text{H}_2$  and  $\text{H}_2$  profiles are also similar showing initially an increase in concentration as a function of axial location followed by a rapid decrease at the higher heights (40 and 70 mm axial locations). However, one major difference involves the magnitude of the  $\text{C}_2\text{H}_2$  mole fractions which are nearly a factor of 8 larger in the ethene flame as compared to the methane flame. This larger concentration of acetylene is consistent with the much more heavily sooting characteristics of the ethene flame. It is interesting to note that the hydrogen mole fractions are quite similar in the two flames (see Figures 3c and 4c) in contrast to the acetylene results.

Looking with more detail at the ethene flame results, one observes the profile of  $\text{C}_2\text{H}_2$  has a broad peak at 7 mm, suggesting that production occurs through much of the fuel rich part of the flame below this height (see Figure 4b). The  $\text{H}_2$  profile at this height, shown in Figure 4c, resembles the profile of the  $\text{C}_2\text{H}_2$ . This is due to the coproduction of both  $\text{C}_2\text{H}_2$  and  $\text{H}_2$  from the fuel. The doubling of the peak mole fraction from 0.03 at 7 mm to 0.06 at 20 mm attests to the continued net production of  $\text{C}_2\text{H}_2$  throughout this region. During this time, the source of acetylene, the ethene

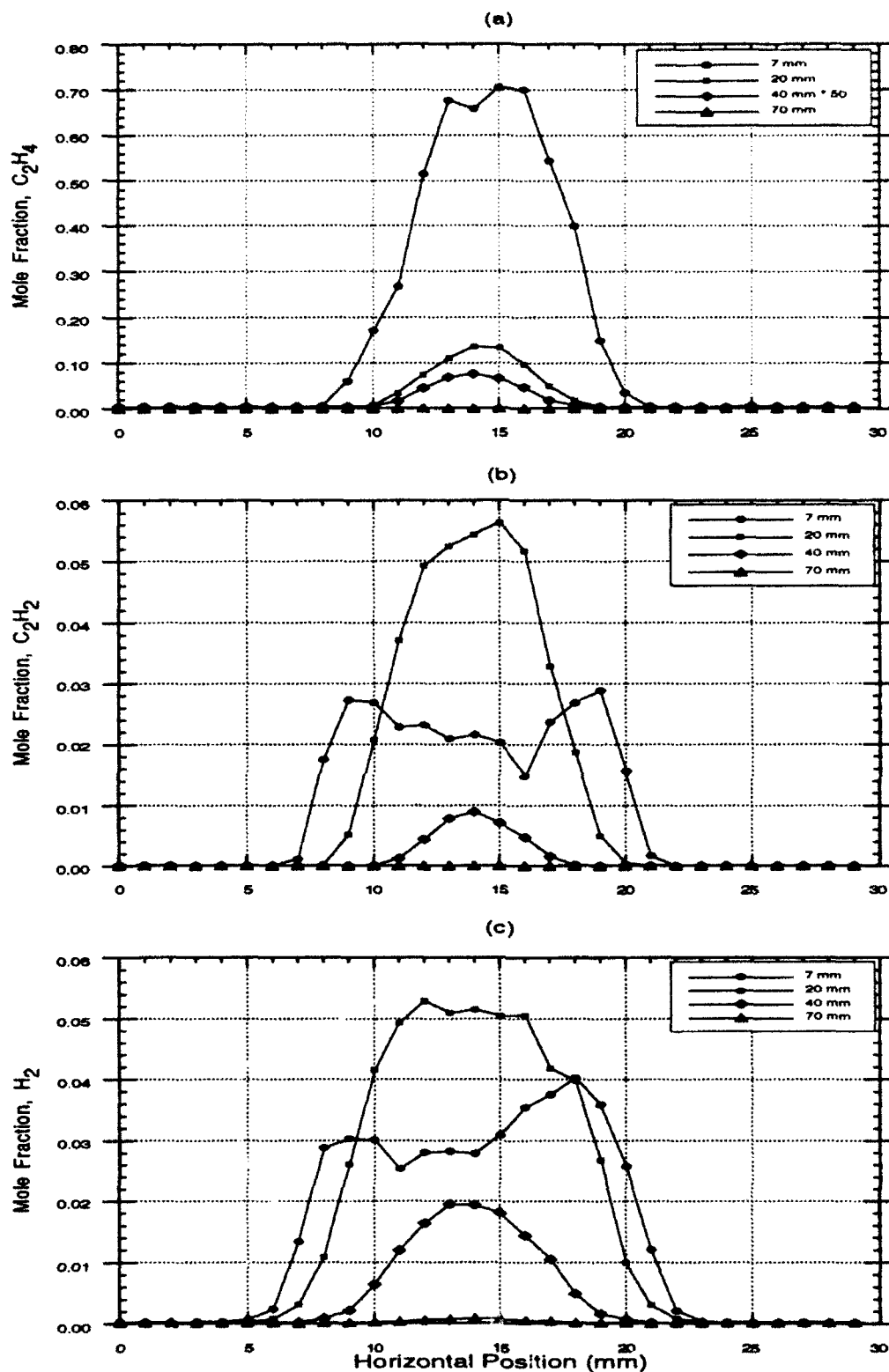


**Figure 4.** Plots of the measured species mole fractions as a function of horizontal position for several axial locations (7, 20, 40 and 70 mm) in a C<sub>2</sub>H<sub>4</sub> / Air diffusion flame with a fuel flow rate of 3.85 cm<sup>3</sup>/s: a) C<sub>2</sub>H<sub>4</sub> mole fractions, b) C<sub>2</sub>H<sub>2</sub> mole fractions, c) H<sub>2</sub> mole fractions.

fuel, has decreased from a peak of 0.7 at 7 mm to 0.14 at 20 mm. Therefore, with the source decreasing, the  $C_2H_2$  peak at 40 mm decreases to 1/6 of its value at 20 mm. This 40 mm height coincides with almost total consumption of the fuel and the location of the greatest local soot volume fraction [4,5]. The total amount of carbon contained as soot at this height represents 14% of the total carbon flow rate, while the major species remaining to be oxidized are  $H_2$  and  $C_2H_2$  with 0.02 and 0.01 mole fractions respectively, and most probably CO.

In addition to  $C_2H_2$  which is argued to be a major surface growth species, measurements of diacetylene ( $C_4H_2$ ) and benzene ( $C_6H_6$ ) were also obtained. Calibrations for these species are not yet available and only the raw signal data will be discussed. Figure 5 shows plots of the  $\mu$  profiles for  $C_4H_2$  and  $C_6H_6$  signal intensities for several axial positions in the ethene flame. The  $C_4H_2$  profiles indicate net production of diacetylene is occurring by the 7 and 20 mm axial locations with the annular region initially favored. Between the 20 and 30 mm axial locations the magnitude of the peak signal intensity remains constant while the profile becomes narrower. This suggests that production of  $C_4H_2$  occurs in the center region of the flame followed by subsequent diffusion to the flame front with consumption nearly balancing the source of  $C_4H_2$  since the profile only changes slightly. Above the 30 mm axial location production rapidly diminishes as compared to consumption and the  $C_4H_2$  concentration decreases significantly by 40 mm. The benzene signals show a somewhat different evolution. Although net production is observed also over the region between the 7 mm and 20 mm axial locations, the only height to indicate distinctive peaks in the annulus is the 7 mm height. Thus, benzene is rapidly formed throughout the center region of the ethene flame in contrast to  $C_2H_2$  and  $C_4H_2$  which initially favor the annular region. The signal intensity has doubled by the 20 mm axial location as compared to the 7 mm axial location, but then decreases by one-half at the 30 mm height. This implies a smaller region where conditions favor net production of  $C_6H_6$ .

By comparing the profiles of  $C_4H_2$  and  $C_6H_6$  one can conclude that the  $C_4H_2$  is formed closer to the high temperature reaction zone. The evidence for this observation is the more

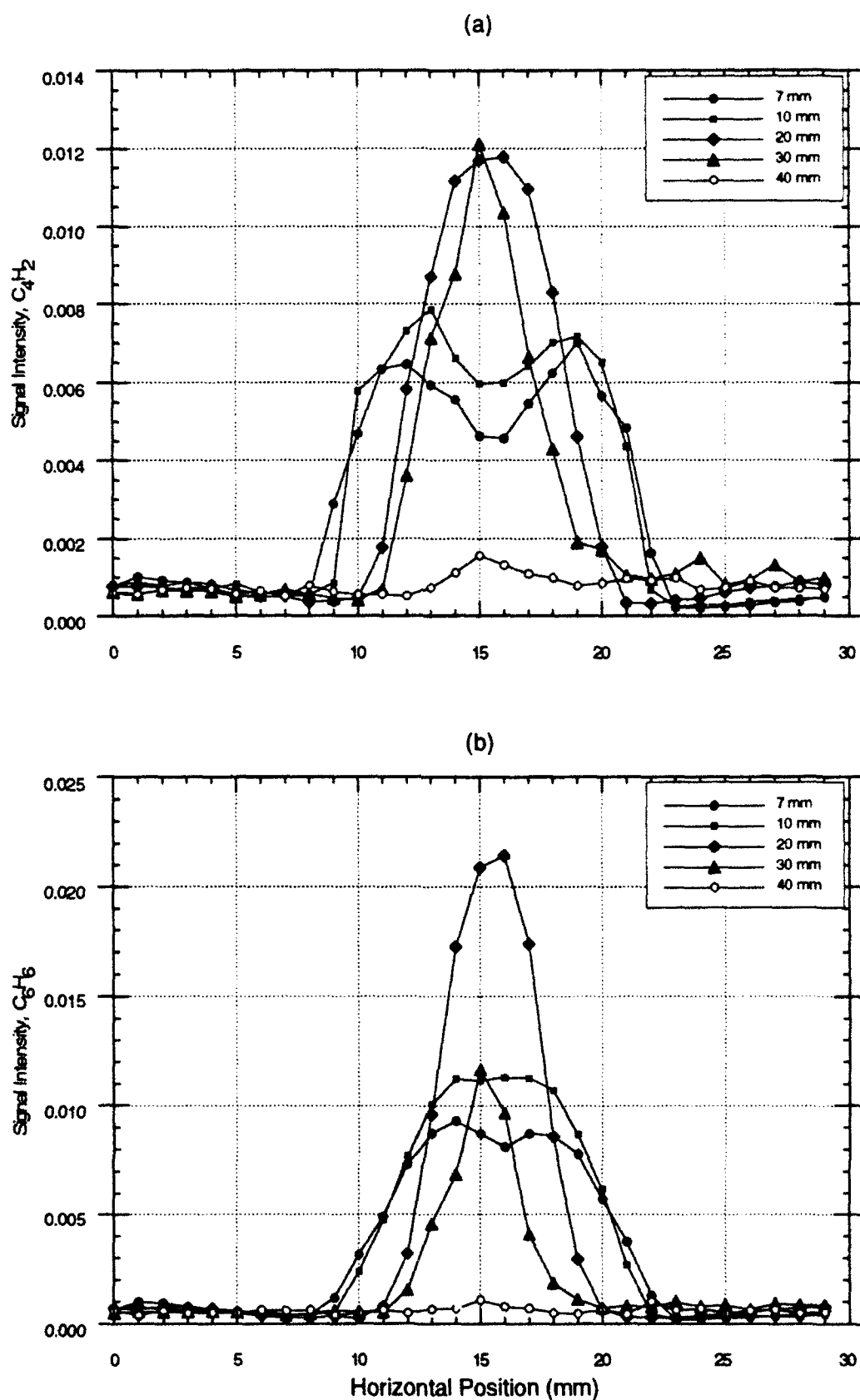


**Figure 5.** Plots of signal intensity for diacetylene and benzene as a function of horizontal position for several axial locations (7, 10, 20, 30 and 40 mm) in a  $C_2H_4/Air$  diffusion flame with a fuel flow rate of  $3.85 \text{ cm}^3/\text{s}$ : a)  $C_4H_2$  signal intensity profiles, b)  $C_6H_6$  signal intensity profiles.

pronounced two peak shape and the wider base and steeper slope towards the reaction zone. These characteristics are most evident at the 7 and 10 mm axial positions. If the structure of  $C_4H_2$  is such that it is more stable and has a faster formation rate at higher temperatures, then there may be continued production to a higher height than  $C_6H_6$ . This could account for the later decay of the  $C_4H_2$  signals as compared to  $C_6H_6$ . Another argument could be that the kinetics involved in the consumption of  $C_6H_6$  to form larger or smaller molecules are faster than for  $C_4H_2$ . In this case the concentration of  $C_6H_6$  would be reduced as compared to  $C_4H_2$ . The resolution of such interesting details remains for future studies planned as part of this program.

As was mentioned earlier an advantage in obtaining species concentration measurements for the ethene/air diffusion flame is the availability of other related measurements [1-10]. In particular, an extensive set of measurements on the evolution of the soot particle field is available along with related temperature and velocity field determinations. From the velocity measurements, soot particles path can be determined and, thus, the detailed evolution of soot particle growth and oxidation can be obtained. In the present case, the soot growth process will be examined in relationship to the acetylene concentration field. In examining this process, three particle paths will be considered. One path includes the region of the flame where the maximum soot volume fraction is observed. A second considers the center line region of the flame while the third involves a particle path located between these other two paths.

Figure 6 shows soot volume fraction  $f_v$ , and the acetylene mole fraction as a function of time along each of these particle paths. These measurements represent the first time that such detailed species concentration information has been available in diffusion flames with accompanying detail soot particle information. Each of the particle paths shows the same trends. The soot volume fraction achieves a maximum at the same location where the acetylene concentration has approached zero. Thus, the depletion of growth species is the reason for soot growth ceasing. In the premixed flames, similar measurements indicate that significant acetylene concentrations exist well after soot growth

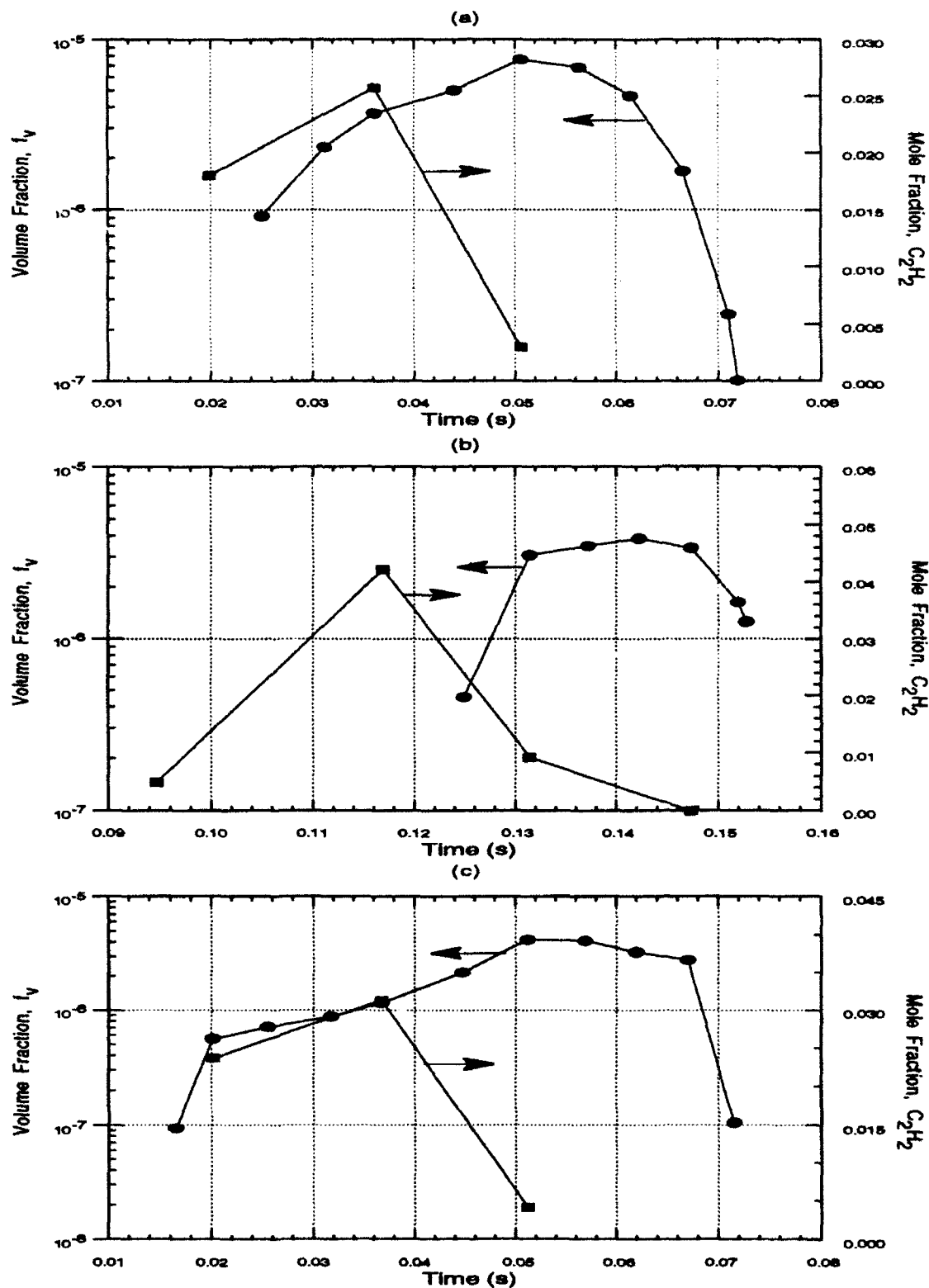


**Figure 6.** Plots of the soot volume fraction,  $f_v$ , and the mole fraction of  $C_2H_2$  as a function of time for a) the particle path containing the maximum soot volume fraction, b) the particle path intermediate to the particle path containing the maximum soot volume fraction and the center line, c) the particle path along the center line.

stops. This observation has been used to argue that decreases in soot particle reactivity are responsible for the termination of soot mass addition. The present measurements for these ethene/air diffusion flames show that in the case of diffusion flames, a different mechanism is operative. This result is quite significant since it rules out one of three possible mechanisms responsible for soot growth ceasing, that is loss of surface reactivity. The other two mechanisms remain to be investigated.

Of the two remaining mechanisms, one involves a decrease in the acetylene concentration because the source of acetylene decreases while the sink for acetylene, surface reactions with soot particles, continues to deplete the acetylene present in the flame. The second mechanism involves the competition between formation and oxidation, that is as higher locations in the flame are achieved, oxidation of intermediates and soot particles reduce the net rates of production. It is quite likely that both mechanisms are important in different parts of the flame.

To fully examine these mechanisms, measurements of only the acetylene concentration are not sufficient. Information on the concentration of oxidizing species is also required. The mass spectrometer measurements do provide a measure of the oxygen ( $O_2$ ) which is present in the flame. Another species of interest is hydroxyl radical (OH) which is known to be important in the oxidation of soot particles and possibly early soot precursors. Recently in our laboratory, laser-induced fluorescence has been utilized to obtain measurements of OH throughout this ethene/air diffusion flame [10].

Figure 7 shows the radial profiles of OH mole fraction at two axial locations in the flame, 7 and 70 mm. The arrows located on the figure indicate the location of the particle path containing the maximum  $f_v$  and the intermediate particle path, while the particle path along the center line lies at  $r$  equal to 0. The particle path containing the maximum  $f_v$  lies at the larger radial position indicated by the arrow. At the lower axial position (see Figure 7a), the particle paths lie inside the region of peak OH concentration and generally experience low concentrations of OH radicals. As the soot particles

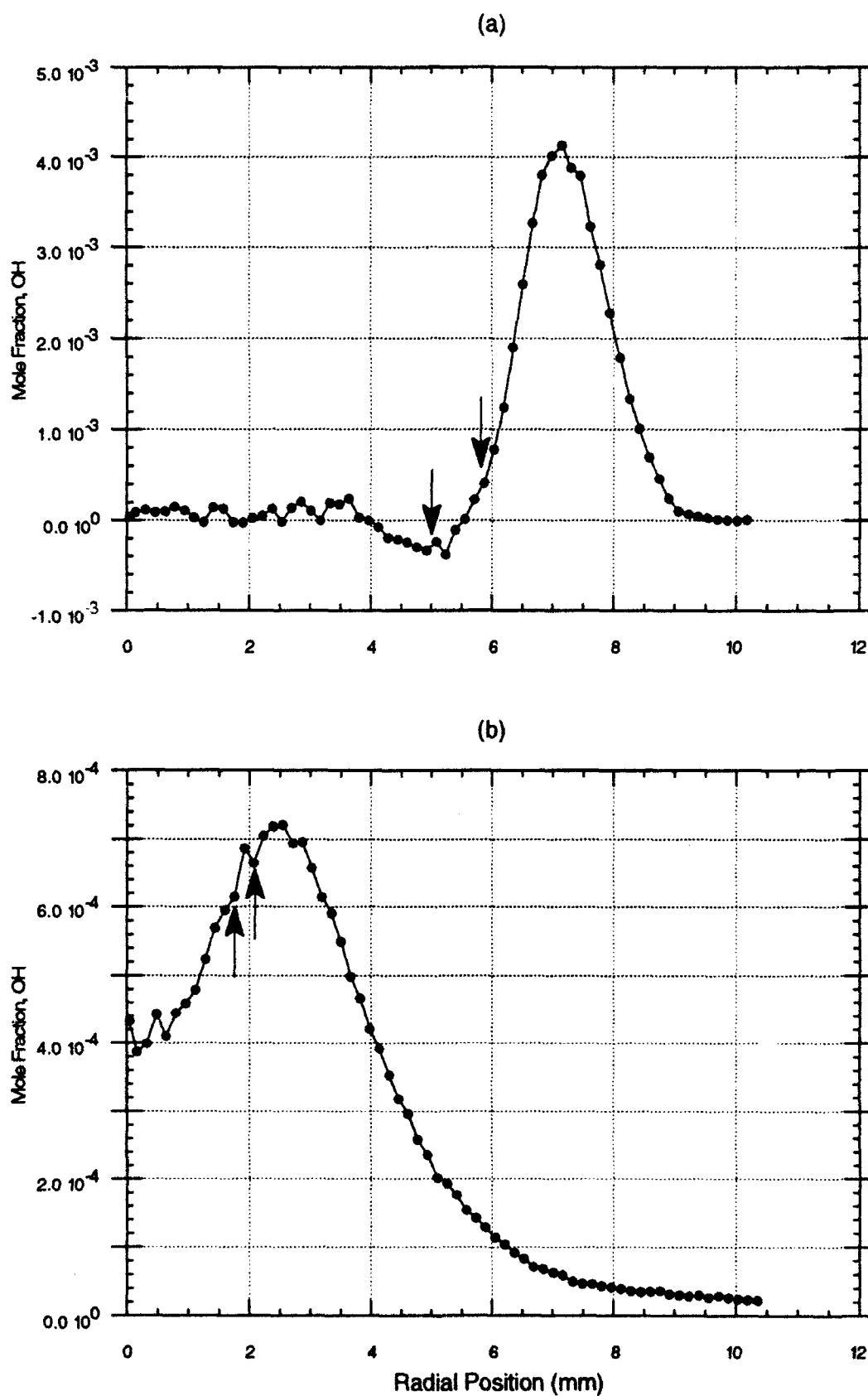


**Figure 7.** Plots of the OH profile for two axial locations in the ethene/air diffusion flame: a) 7 mm axial location, b) 70 mm axial location. Note arrows indicate where the particle paths discussed in Figure 6 intersect the profiles. Negative values for the OH mole fraction are a result of subtraction errors in analyzing the data.

traverse the flame and reach higher locations, larger OH concentrations are observed in regions where soot particles occur. At these higher axial locations, these OH concentrations contribute to reactions resulting in particle oxidation. These results clearly indicate that OH concentrations can also be particle path resolved in these flames. This analysis is currently on-going and will be combined with the previously described species concentration measurements to investigate the oxidative competition which occurs involving both gas phase species such as  $C_2H_2$  as well as the soot particles.

In summary, the present investigations have added critical new data needed to establish the mechanism controlling soot growth and oxidation. In particular, the measurements of  $C_2H_2$  have revealed that soot surface growth ceases due to the depletion of growth species not due to the loss of soot particle reactivity. This observation is in agreement with recent work by Honnery and Kent [19,20], who have shown that in long laminar diffusion flames, soot growth can be extended to very long residence times. The species measurements now need to be combined with complementary soot particle, temperature and OH field measurements to examine other mechanistic questions. Additionally, other fuels should be studied as well in order to take advantage of the previous work done in our laboratory on fuel structure effects.

### 3.2 Laser-Induced Fluorescence Measurements of PAH Species

As described earlier, a laser-induced fluorescence technique (LIF) is being utilized to follow the evolution of the PAH species in these laminar diffusion flame studies of soot formation. This technique is more qualitative in nature than the mass spectrometric concentration measurements described in the previous section. In fact, the LIF measurements are intended to provide complementary information to the mass spectrometer results regarding the growth of large aromatic hydrocarbons which exceed the mass range of that instrument. The principle for these LIF studies involves obtaining fluorescence measurements as a function of the excitation wavelength of the laser throughout the flame. Additionally, the fluorescence intensity is measured at several wavelengths to characterize the spectrum of the fluorescing species. To illustrate the characteristics of this approach,

Figure 8 shows the fluorescence signals observed at an axial location 7 mm above the exit of the burner for a single excitation wavelength ( $\lambda_o = 283.5$  nm). Each of the profiles shown in Figure 8 represents the fluorescence collected at a different wavelength using narrow-band filters centered at the indicated wavelength with a 10 nm bandpass. From this figure, one observes that the shortest wavelength region measured ( $\lambda_f = 334$  nm) reaches a maximum nearest to the center line while longer wavelength fluorescence signals peak at larger radial locations. The shift in the fluorescence is a result of the changing composition of the species fluorescing with the longer wavelengths being associated with larger PAH species [21]. Note also that the double peaked structure exhibited by the fluorescence signals is similar to that observed in the diacetylene and acetylene profiles observed with the mass spectrometer measurements. The interpretation of these results is that the signals observed at shorter wavelengths (e.g.,  $\lambda_f = 334$  nm) represent the early, smaller PAH precursors to soot particles, while those observed at longer wavelengths (e.g.,  $\lambda_f = 600$  nm) represent larger PAH species formed just prior to soot particle inception. One should note that in these ethene/air flames soot particles first appear at a radial location near 5 mm from the center line at an axial location of 7 mm which corresponds roughly to the observed position for fluorescence signals at longer wavelengths.

Figures 9-11 illustrate this point further and provide additional examples of the information which can be obtained from these LIF studies. These figures also show fluorescence signal profiles obtained with an excitation wavelength ( $\lambda_o$ ) of 283.5 nm as a function of axial location (7, 10, 20 and 30 mm) for three regions of the observed fluorescence spectra,  $\lambda_f = 334$  nm, 420 nm and 600 nm, for Figures 9, 10 and 11, respectively. Figure 9 shows that the fluorescence observed at 334 nm is a maximum at the 7 mm axial location and then decreases to nearly constant values at the higher axial locations of 10, 20 and 30 mm. However, for the longer wavelength ( $\lambda_f = 420$  nm and 600 nm) fluorescence signals, a continual increase in the signal is observed as the axial height increases. The signals observed at  $\lambda_f = 420$  nm are greater than those for the other two wavelengths. The general

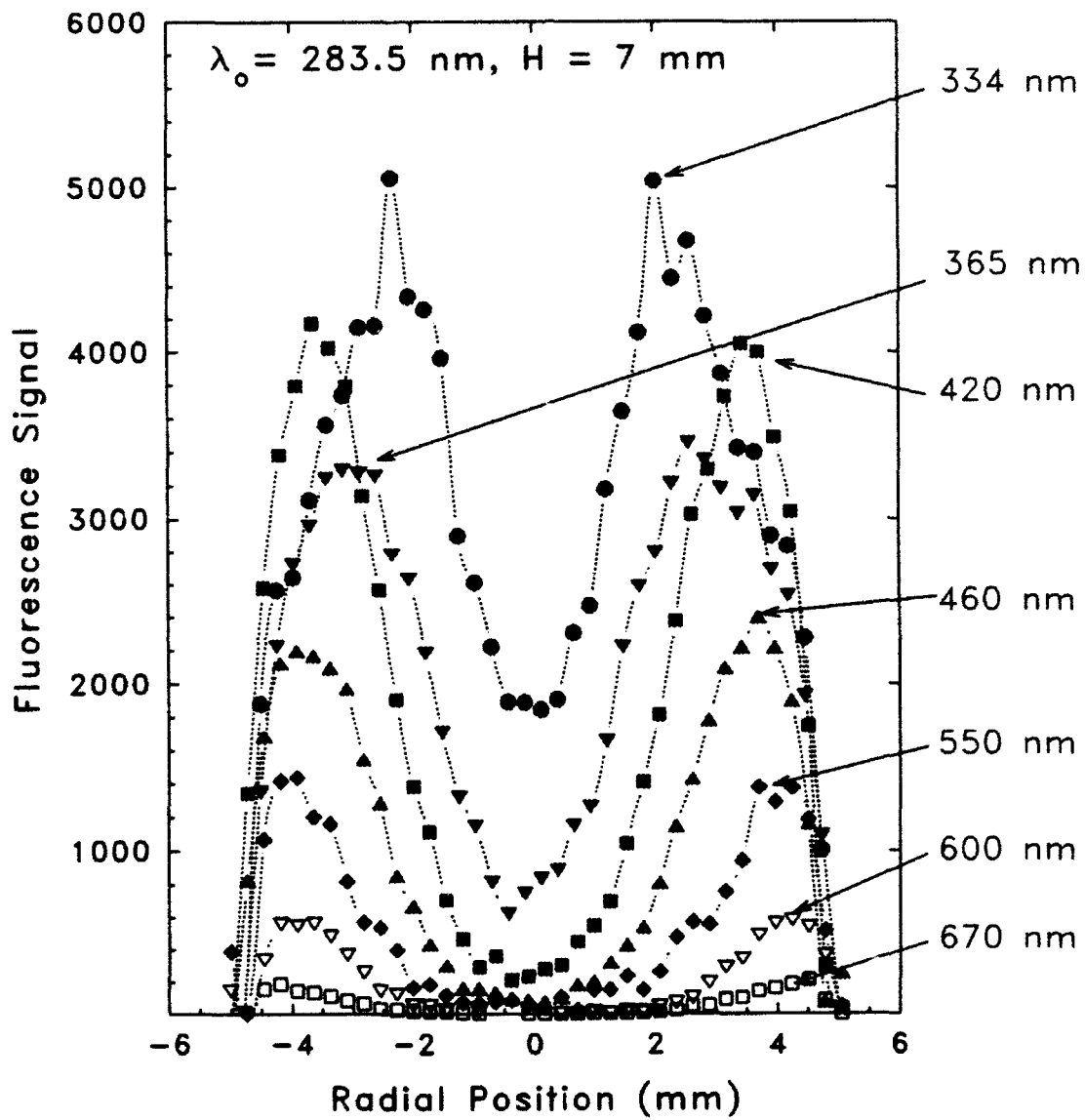
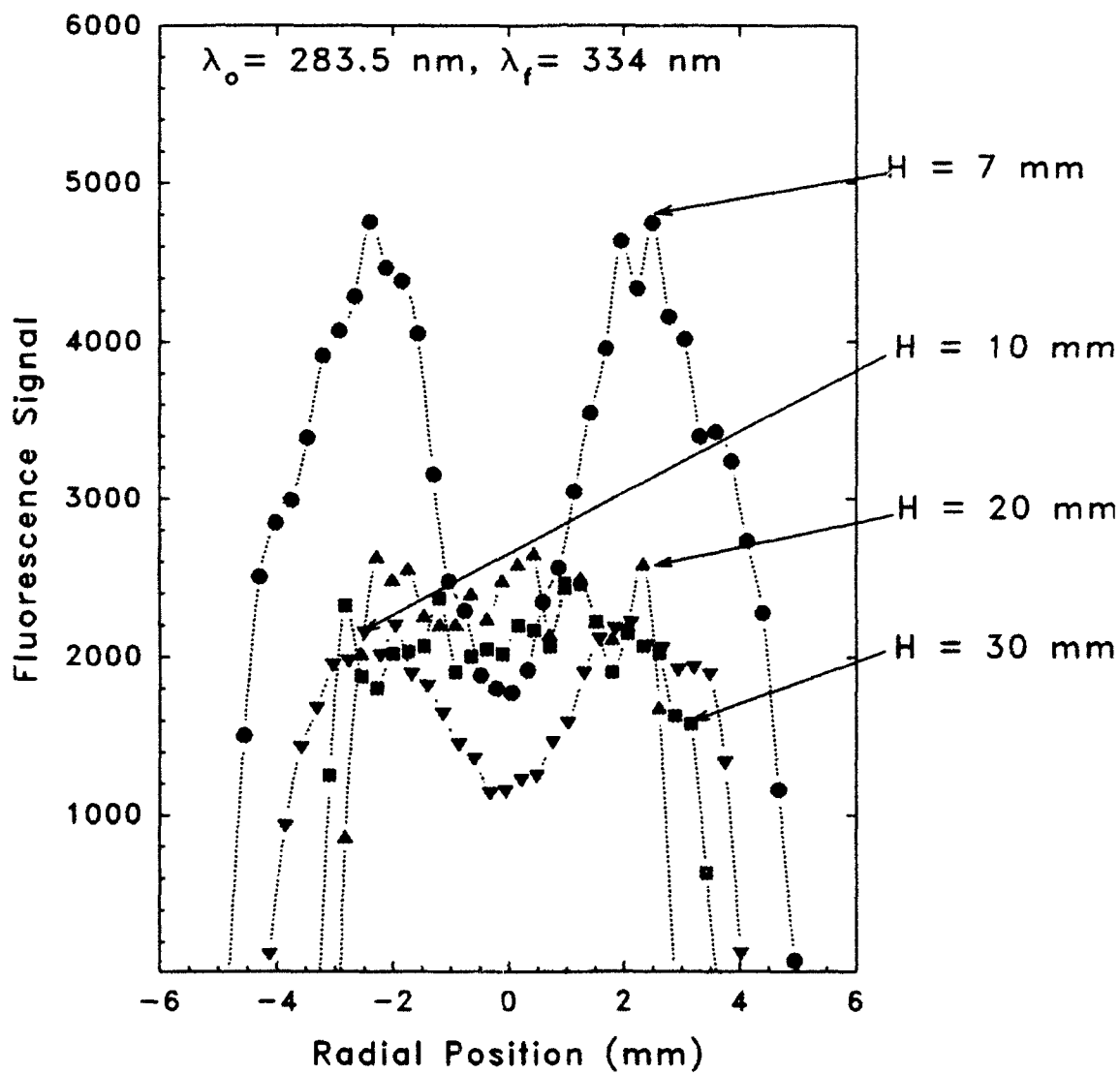


Figure 8. Fluorescence signal intensity as a function of radial position and fluorescence wavelength ( $\lambda_f$ ) for an excitation wavelength,  $\lambda_o$ , of 283.5 nm at an axial location of 7 mm above the burner exit.



**Figure 9.** Fluorescence signal intensity as a function of radial position for four axial locations 7, 10, 20 and 30 mm above the burner exit. The laser excitation wavelength,  $\lambda_o$ , is 283.5 nm and the fluorescence detection wavelength,  $\lambda_f$ , is 334 nm.

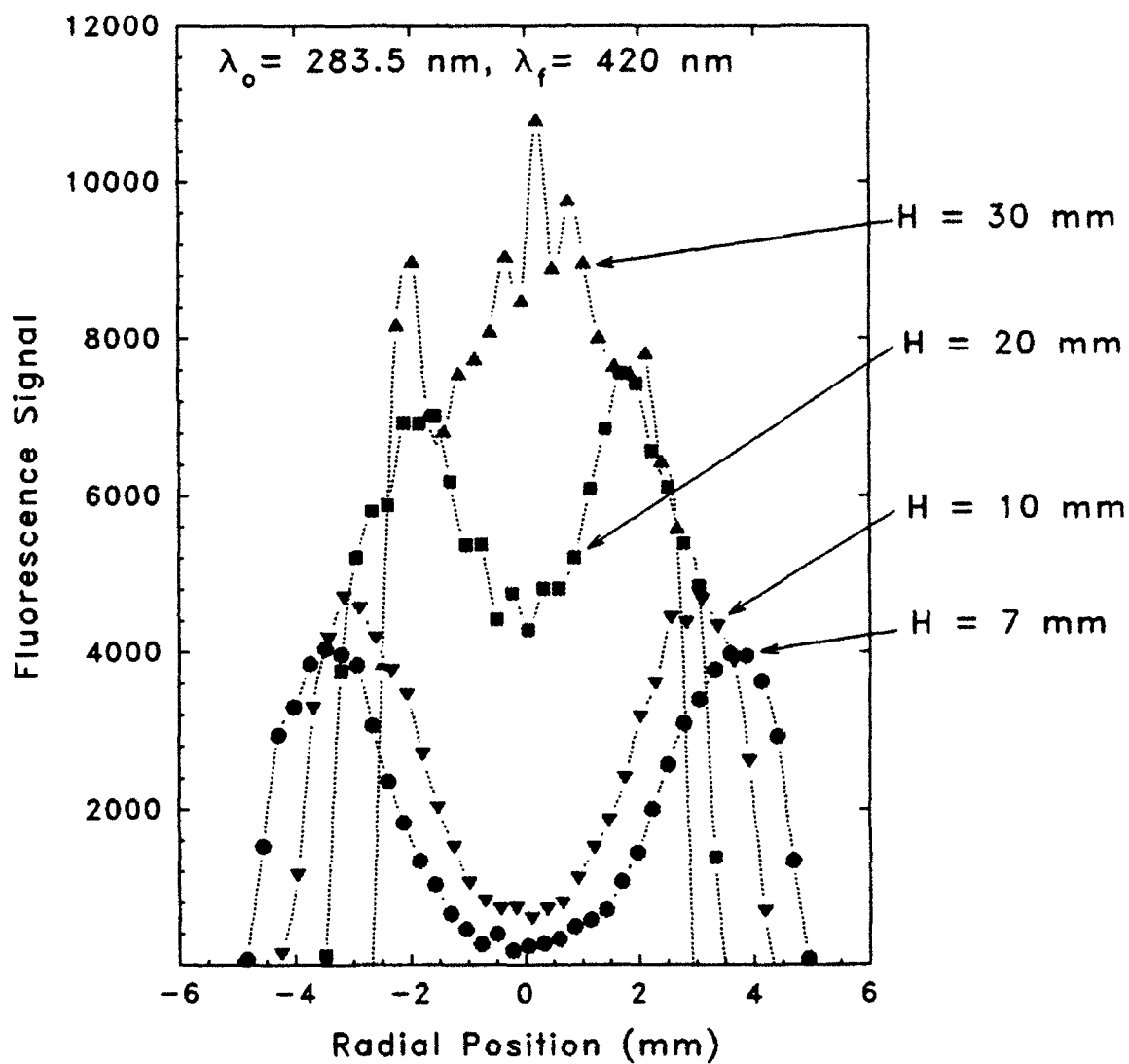


Figure 10. Fluorescence signal intensity as a function of radial position for four axial locations (7, 10, 20 and 30 mm) above the burner exit. The laser excitation wavelength,  $\lambda_o$ , is 283.5 nm and the fluorescence detection wavelength,  $\lambda_f$ , is 420 nm.

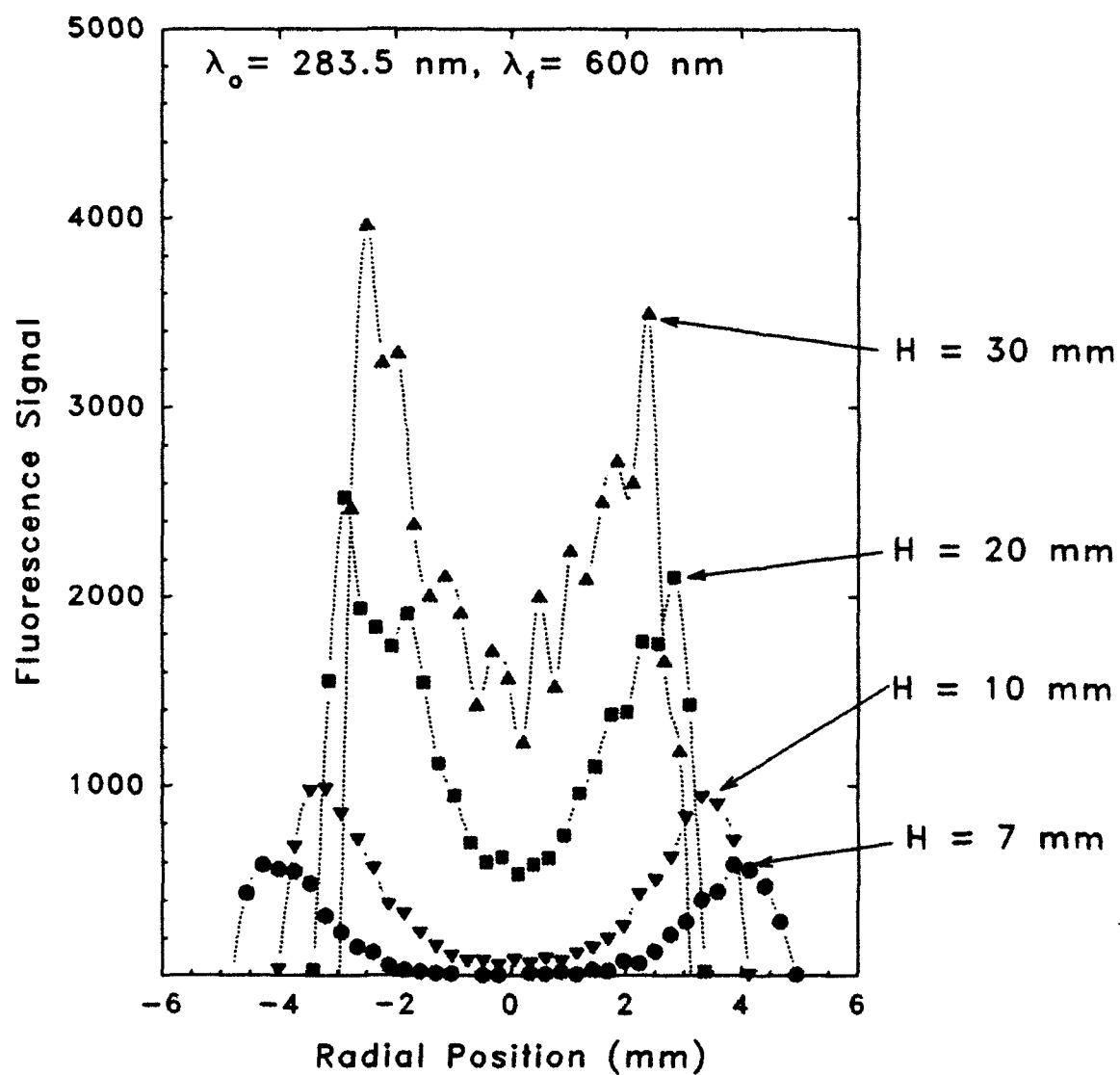
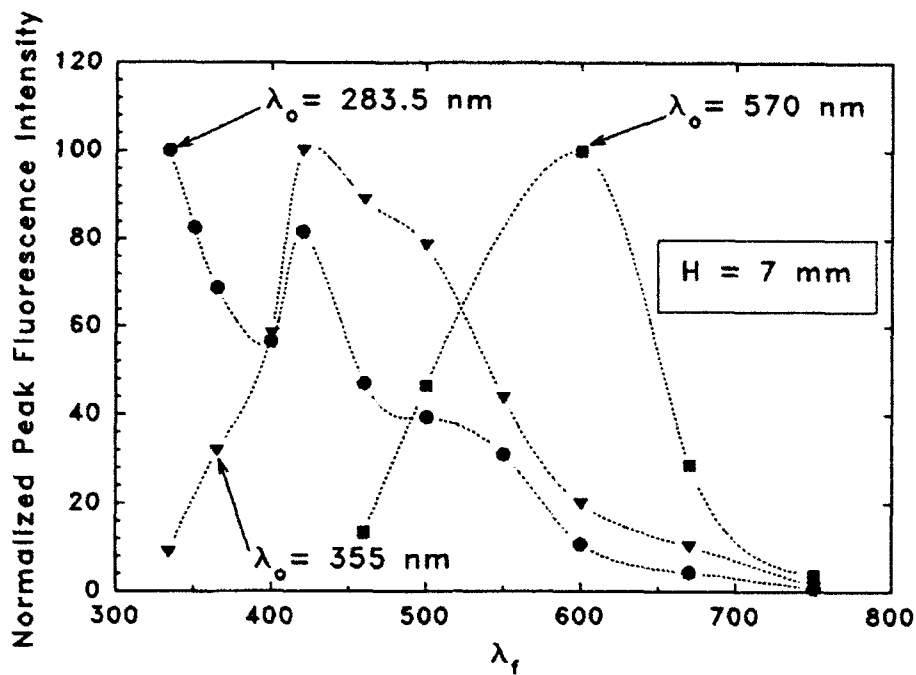


Figure 11. Fluorescence signal intensity as a function of radial position for four axial locations (7, 10, 20 and 30 mm) above the burner exit. The laser excitation wavelength,  $\lambda_o$ , is 283.5 nm and the fluorescence detection wavelength,  $\lambda_f$ , is 600 nm.

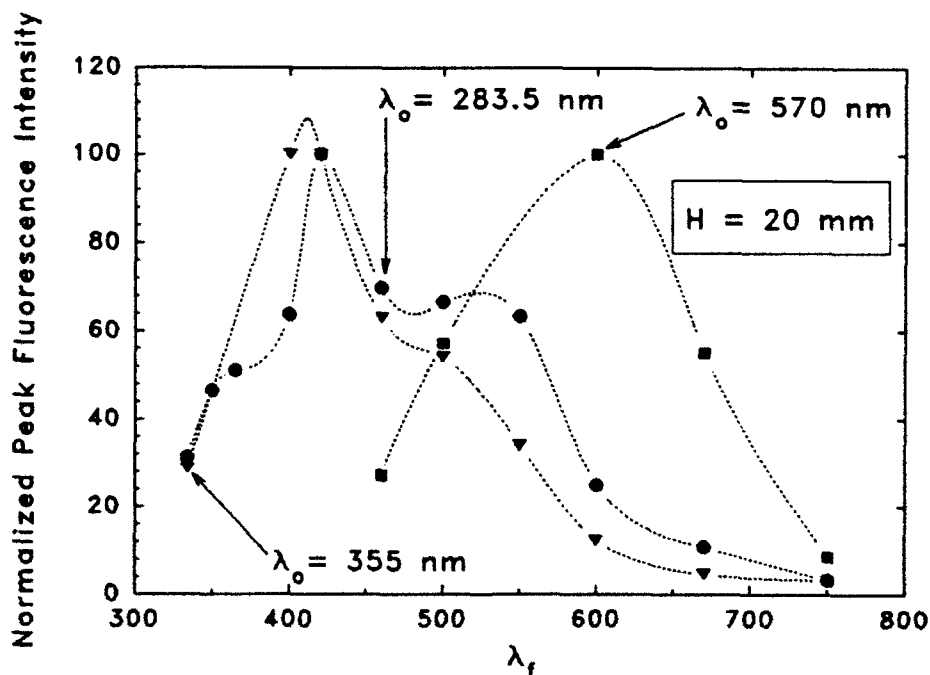
trend is to maintain the double peak structure with the exception of the 30 mm axial location for the  $\lambda_f = 420$  nm profile which peaks near the center line. The profiles are broader radially as the observed fluorescence wavelength is increased from  $\lambda_f = 334$  nm to  $\lambda_f = 600$  nm in agreement with the trends shown in Figure 8 for the 7 mm axial location. Again, these results are interpreted to indicate the relative growth of small PAH species (shorter  $\lambda_f$  wavelengths) as compared to large PAH species (longer  $\lambda_f$  wavelengths). Thus, these measurements allow us to track broadly the evolution of the PAH species. Such data can be used to compare to the growth patterns predicted from modeling studies for PAH species [11].

Additional information can be gained from varying the excitation wavelength. Figure 12 shows the normalized peak fluorescence spectra observed for three different excitation wavelengths ( $\lambda_o = 283.5$  nm, 355 nm and 570 nm). Two axial locations (7 mm and 20 mm) are shown as well. Significant differences in the shape of the spectra are observed between spectra obtained with different excitation wavelengths. Again, the interpretation is that longer excitation wavelengths favor larger PAH species over smaller species. In comparing the spectra obtained at different axial locations (compare Figure 12a and b), the largest differences are observed for the spectra obtained with the shorter excitation wavelengths ( $\lambda_o = 283.5$  nm and 355 nm). These differences indicate that the relative compositional mix of the PAH species is changing with location. The degree to which species specific information can be obtained remains to be ascertained. Nonetheless a wealth of qualitative information on species evolution is available from these measurements.

Finally, Figure 13 shows the maximum fluorescence intensity as a function of axial position for several fluorescence wavelengths using an excitation wavelength of  $\lambda_o = 355$  nm. The trend is quite clear in that the fluorescence signals increase with increasing height until near the 20 mm location after which the signals decrease with the exception of the  $\lambda_f = 600$  nm fluorescence signals which stays nearly constant above 20 mm. The maximum intensity occurs for the  $\lambda_f = 400$  nm region of the spectrum.



(a)



(b)

Figure 12. The normalized peak fluorescence intensity as a function of fluorescence detection wavelength,  $\lambda_f$ , for laser excitation wavelengths of 283.5, 355 and 570 nm: a) 7 mm axial location above the burner exit, b) 20 mm axial location above the burner exit.

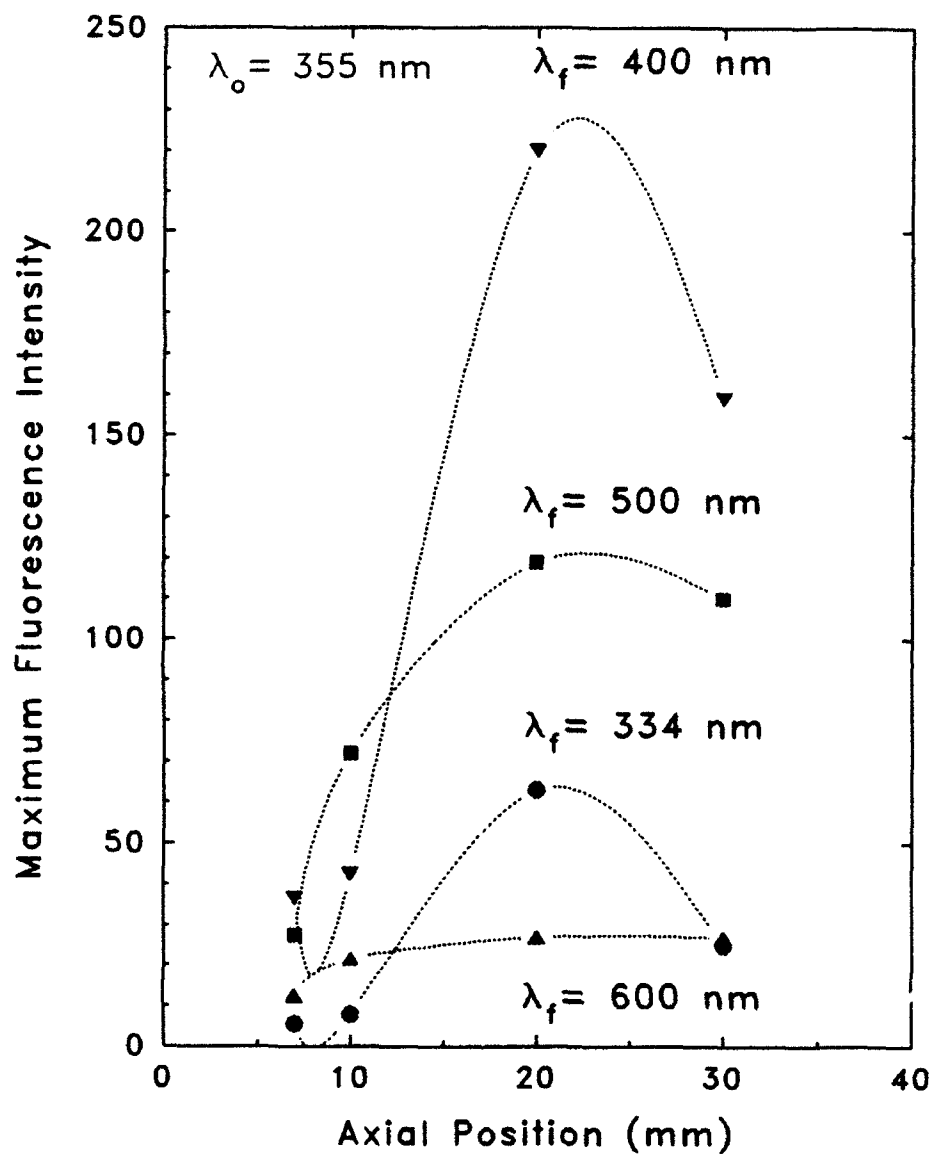


Figure 13. The maximum fluorescence intensity as a function of axial position for laser excitation wavelength,  $\lambda_o$ , of 355 nm and fluorescence detection wavelengths of 334, 400, 500 and 600 nm.

All of these trends show great potential in leading to further insights into the soot formation process. However, the true value of this approach will depend on quantifying these results at least on a relative scale and extending them to a wider range of fuel conditions.

In summary, the LIF measurements of PAH fluorescence have shown that the resulting fluorescence spectra are quite sensitive to the laser excitation wavelength. Furthermore, through variation of the wavelength at which the fluorescence signal is measured, a systematic structure to the fluorescence signal profiles is observed. This structure is argued to be due to changes in the molecular weight (i.e., size) of the PAH species responsible for the observed fluorescence. Thus, the LIF measurements have the potential to follow qualitatively the increase in molecular size throughout the flame. The degree to which quantitative measurements of specific classes of PAH species can be identified is a goal for the next year of the current program.

### **3.3 Aerosol Dynamic Processes of Soot Aggregates in Diffusion Flames**

Soot formed in flames usually consists of aggregates (clusters or agglomerates) of a variable number of nearly spherical, monodisperse primary particles (monomers or spherules). In the present work, the optical properties of polydisperse aggregates are used to analyze light scattering data from a coannular ethene diffusion flame. In previously reported studies, data have been obtained on the local extinction and volumetric scattering cross sections from laser scattering experiments, on the flame velocity field from laser velocimetry, and on the primary particle sizes determined by electron microscope [22]. The present analysis involves laser scattering/extinction tests on a coannular ethene diffusion flame using cross sections for polydisperse aggregates. Using an improved experimental arrangement that allowed simultaneous measurement of light scattering at multiple angles, it was possible to determine the fractal dimension of the aggregates in the flame. The analysis also yields the mean-square radius of gyration, the aggregate number concentration, the average number of primary particles per aggregate, as well as the volume average of the concentration in this flame. These results lead to the conclusion that soot aerosol dynamic processes in the laminar ethene flame

are partitioned into four regions. Low in the diffusion flame there is a region of particle inception that establishes the number of primary particles per unit volume that remains constant along a prescribed soot path line. In the second region, there is sustained particle growth through the combined action of cluster-cluster aggregation (CCA) accompanied by heterogeneous reactions contributing to monomer-cluster growth. Oxidation processes occur in the third region where CCA continues. If aggregate burnout is not complete in the oxidation region, then smoke is released to the surroundings in the fourth region where reactions cease but clusters continue to grow by CCA. The experiments yield the CCA growth rate within the flame which compares favorably with the theoretical value.

A more complete treatment of this topic is contained in Appendix A, which contains a reprint of a recent article published in *Combustion and Flame*.

#### 4.0 Conclusions

Results obtained during the first year of the current research program have shown that spatially resolved measurements of several key gas phase intermediates important in soot formation can be measured. Using a novel sampling probe approach, species concentrations have been measured throughout the fuel-rich particle laden region of diffusion flames. Of particular importance have been the results for the acetylene concentration. When combined with previously obtained soot particle field measurements, it has been possible to establish that soot particle surface growth ceases due to the depletion of surface growth reactants, not because of a loss of soot particle surface reactivity. This result is in contrast to premixed flame results where significant amounts of acetylene remain even after soot growth stops.

Measurements of polynuclear aromatic species using a laser-induced fluorescence technique have demonstrated a strong sensitivity of the fluorescence signals to the excitation and detection wavelength conditions utilized. These results have been interpreted as a means to qualitatively follow

the growth of large molecular species in the flame. Future work needs to concentrate on making these results more quantitative in nature.

Work has also continued on examining the effects of soot aggregates on the interpretation of light scattering measurements of soot particle properties. A self-consistent formulation of the light scattering cross section of aggregated particles has been developed. The impact of these aggregate structures on the interpretation of light scattering results has been examined.

Future work on this program will extend the current measurements to a wider range of fuel structures and will examine the role of oxidation on the depletion of key surface growth species. Efforts will also continue on furthering the quantitative interpretation of the PAH fluorescence results.

#### 5.0. References

1. Santoro, R. J., "Fuel Structure and Pressure Effects on the Formation of Soot Particles in Diffusion Flames," AFOSR-TR-88-0664, 1989.
2. Richardson, T. F. and Santoro, R. J., "Soot Formation in Coannular Diffusion Flames: The Effect of Fuel Dilution with Inert Species," submitted to *Combustion Science and Technology* (1992).
3. Puri, R. and Santoro, R. J., "The Role of Soot Particle Formation on the Production of Carbon Monoxide in Fires," *Fire Safety Science Proceedings of the Third International Symposium*, Elsevier Applied Science, London, pp. 595-604 (1991).
4. Santoro, R. J., Semerjian, H. G. and Dobbins, R. A., "Soot Particle Measurements in Diffusion Flames," *Combustion and Flame*, 52, pp. 204-218 (1983).
5. Santoro, R. J., Yeh, T. T., Horvath, J. J. and Semerjian, H. G., "The Transport and Growth of Soot Particles in Laminar Diffusion Flames," *Combustion Science and Technology*, 53, p. 89 (1987).
6. Santoro, R. J., "Fuel Molecular Structure Effects on Soot Particle Growth in Diffusion Flames," *Twentieth Fall Technical Meeting of the Eastern Section of The Combustion Institute*, Paper #19, Gaithersburg, MD, Nov. 2-5, 1987.
7. Richardson, T. F. and Santoro, R. J., "Soot Growth in Diffusion Flames Burning Fuel Mixtures," *Twenty-First Fall Technical Meeting of the Eastern Section of The Combustion Institute*, Paper #44, Clearwater Beach, FL, Dec. 5-7, 1988.
8. Santoro, R. J., "Optical Measurements of Soot Particles in Flames," *Mat. Res. Soc. Symp. Proc.*, 117, pp. 157-163 (1988).

9. Puri, R., Richardson, T. F., Santoro, R. J. and Dobbins, R. A., "Aerosol Dynamic Processes of Soot Aggregates in a Laminar Ethene Diffusion Flame," *Combustion and Flame*, 92, pp. 320-333 (1993).
10. Puri, R., Moser, M., Santoro, R. J. and Smyth, K. C., "Laser-Induced Fluorescence Measurements of OH Concentration in the Oxidation Region of Laminar, Hydrocarbon Diffusion Flames," *Twenty-Fourth Symposium (International) on Combustion*, The Combustion Institute, Pittsburgh, PA, pp. 1015-1022 (1992).
11. Frenklach, M. and Wang, H., "Detailed Modeling of Soot Particle Nucleation and Growth," *Twenty-Third Symposium (International) on Combustion*, The Combustion Institute, Pittsburgh, PA, pp. 1559-1566 (1990).
12. Smooke, M. D., Lin, P., Lam, J. K. and Long, M. B., "Computational and Experimental Study of a Laminar Axisymmetric Methane-Air Diffusion Flame," *Twenty-Third Symposium (International) on Combustion*, The Combustion Institute, Pittsburgh, PA, pp. 575-582 (1990).
13. Kennedy, I. M., Kollmann, W. and Chen, H.-Y., "A Model for Soot Formation in Laminar Diffusion Flames," *Combustion and Flame*, 81, pp. 73-85 (1990).
14. Megaridis, C. M. and Dobbins, R. A., "Comparison of Soot Growth and Oxidation in Smoking and Non-Smoking Ethylene Diffusion Flames," *Combustion Science and Technology*, 66, pp. 1-16 (1989).
15. Smyth, K. C., Miller, J. H., Dorfman, R. C., Mallard, W. G. and Santoro, R. J., "Soot Inception in a Methane/Air Diffusion Flame as Characterized by Detailed Species Profiles," *Combustion and Flame*, 62, pp. 157-181 (1985).
16. Puri, R. and Santoro, R. J., "Sonic Probe Sampling in Particle Laden Combustion Flows," *Twenty-Third Fall Technical Meeting of the Eastern Section of The Combustion Institute*, Orlando, FL, Dec. 3-5, 1990.
17. Mitchell, R. E., Sarofim, A. F. and Clomburg, L. A., "Experimental and Numerical Investigation of Laminar Diffusion Flames," *Combustion and Flame*, 37, pp. 227-244 (1980).
18. Puri, R., "The Interaction of Soot Particles and Carbon Monoxide in Laminar Diffusion Flames," Ph.D. Thesis, The Pennsylvania State University (1992).
19. Honnery, D. R. and Kent, J. H., "Soot Formation in Long Ethylene Diffusion Flames," *Combustion and Flame*, 82, p. 426 (1990).
20. Kent, J. H. and Honnery, D. R., "Soot Formation Rates in Diffusion Flames - A Unifying Trend," *Combustion Science and Technology*, 75, p. 169 (1991).
21. Petarca, L. and Marconi, F., "Fluorescence Spectra and Polycyclic Aromatic Species in a N-Heptane Diffusion Flame," *Combustion and Flame*, 78, pp. 308-325 (1989).
22. Dobbins, R. A., Santoro, R. J. and Semerjian, H. G., "Analysis of Light Scattering from Soot Using Optical Cross Sections for Aggregates," *Twenty-Third Symposium (International) on Combustion*, The Combustion Institute, pp. 1525-1532 (1990).

## 6.0 Publications

1. Santoro, R. J. and Richardson, T. F., "Concentration and Temperature Effects on Soot Formation in Diffusion Flames," accepted for publication by Springer Verlag in *Mechanisms and Models of Soot Formation* (in press).
2. Puri, R., Richardson, T. F., Santoro, R. J. and Dobbins, R. A., "Aerosol Dynamic Processes of Soot Aggregates in a Laminar Ethene Diffusion Flame," *Combustion and Flame*, 92, pp. 320-333 (1993).
3. Richardson, T. F. and Santoro, R. J., "Soot Formation in Coannular Diffusion Flames: The Effect of Fuel Dilution with Inert Species," submitted to *Combustion Science and Technology*.

## 7.0 Meetings and Presentations

"Laser Diagnostic Measurements of Spray Atomization and Soot Formation Processes," invited seminar NASA Lewis Research Center, February 25, 1992.

"Soot Formation - Progress and Challenges," invited seminar Yale University, April 15, 1992.

"Soot Formation - Progress and Challenges," invited seminar Allison Gas Turbines, February 11, 1993.

"The Effects of Operating Pressure on Soot Formation in Laminar Diffusion Flames," Combustion Fundamentals and Applications, Joint 1993 Meeting of the Central and Eastern States Sections of The Combustion Institute, accepted for presentation March 15-17, 1993.

## 8.0 Participating Professionals

Dr. Robert J. Santoro, Professor of Mechanical Engineering

Mr. Rahul Puri, Graduate Student, Department of Mechanical Engineering (Ph.D. 9/92, accepted position Allison Gas Turbine)

Mr. Thomas Richardson, Graduate Student, Department of Mechanical Engineering (Ph.D. 5/93, accepted position at Allison Gas Turbine).

Mr. Darrell Rapp, Graduate Student (AFRAPT), Department of Mechanical Engineering (Ph.D. expected 6/94).

Mr. Bryan Quay, Graduate Student (ASSERT), Department of Mechanical Engineering (Ph.D. expected 6/96).

Dr. Wonnam Lee, Research Associate

Mr. Daniel Boone, Technician

## 9.0 Interactions

A number of researchers have directly used the extensive data set developed as part of this work to compare with or extend their own research. Some of those who have been directly provided data include:

Professor R. A. Dobbins, Brown University, Providence, RI  
 Dr. R. Hall, United Technologies Research Center, East Hartford, Ct  
 Dr. R. Davis, the National Institute of Standards and Technology, Gaithersburg, MD  
 Dr. P. Solomon, Advanced Fuel Research, Inc., East Hartford, CT  
 Dr. I. Kennedy, University of California, Davis, CA  
 Drs. C. Merkle and S. Turns, The Pennsylvania State University, University Park, PA  
 Dr. H. Mongia, Allison Gas Turbine Division-GM, Indianapolis, IN  
 Dr. K. Smyth, National Institute of Standard and Technology, Gaithersburg, MD  
 Dr. G. Mulholland, National Institute of Standards and Technology, Gaithersburg, MD

In addition to the interactions resulting from interest in soot particle data, there have been interactions with researchers on particle diagnostic problems. In some cases this has resulted in direct visits to particular laboratories to assist in solving these problems. These interactions include:

Dr. M. Zachariah, The National Institute of Standards and Technology, Gaithersburg, MD  
 Dr. Valerie Lyons, NASA-Lewis Research Center, Cleveland, OH  
 Dr. Alan Scaroni, Penn State University, University Park, PA

Several other interactions have also occurred through a general interest in the work supported by AFOSR with:

Columbian Chemical Company, Monroe, LA  
 Cummins Engine Company, Columbus, IN  
 E. I. DuPont De Nemours, Wilmington, De  
 Eastman Kodak, Rochester, NY  
 Allison Gas Turbine Division  
 Cummins Engine, Inc., Columbus, IN  
 Lubrizol, Wickliffe, OH

DuPont is currently supporting work on titanium dioxide particle formation as a direct result of the AFOSR research program. A student, Peter Strakey, has spent two summers with DuPont exchanging expertise and technology developed as part of this research.

Recent work with Allison Gas Turbine Division involving the incorporation of a revised soot model in their gas turbine combustion codes also occurred as a result of the present work. Mr Darrell Rapp, who is an AFRAPT participant, has spent two summers working at Allison on the implementation of that model. This work is an attempt to directly transfer the results of our work to industry. We are now pursuing a separate project on soot reduction on gas turbine engines for which separate funding will be requested as a collaborative activity between Allison Gas Turbine and Penn State.

We have also previously participated by invitation in two international workshops on soot formation:

"Current Problems in Soot Formation During Combustion, : sponsored by The Commission on Condensation Phenomena of the Academy of Science, held in Gottingen, Germany, March 20-30, 1989.

"Mechanisms and Models of Soot Formation--An International Workshop," sponsored by Volkswagen, Heidelberg, Germany, September 29 - October 2, 1991.

**Appendix A: Aerosol Dynamic Processes of Soot Aggregates in a Laminar Ethene Diffusion Flame**

by

**R. Puri, T. F. Richardson, R. J. Santoro and R. A. Dobbins**

## Aerosol Dynamic Processes of Soot Aggregates in a Laminar Ethene Diffusion Flame

R. PURI, T. F. RICHARDSON, and R. J. SANTORO

Department of Mechanical Engineering, Pennsylvania State University, University Park, PA 16802

R. A. DOBBINS

Division of Engineering, Brown University, Providence, RI 02912

Laser scattering/extinction tests on a coannular ethene diffusion flame were analyzed using cross sections for polydisperse aggregates. Using an improved experimental arrangement that allowed simultaneous measurement of light scattering at multiple angles, it was possible to determine the fractal dimension of the aggregates in the flame. The analysis also yields the mean-square radius of gyration, the aggregate number concentration, the average number of primary particles per aggregate, as well as the volume average of the volume-mean diameter as a function of height or residence time along the particle path of maximum soot concentration in this flame. These results lead to the conclusion that soot aerosol dynamic processes in the laminar ethene flame are partitioned into four regions. Low in the diffusion flame there is a region of particle inception that establishes the number of primary particles per unit volume that remains constant along a prescribed soot pathline. In the second region, there is sustained particle growth through the combined action of cluster-cluster aggregation (CCA) accompanied by heterogeneous reactions contributing to monomer-cluster growth. Oxidation processes occur in the third region where CCA continues. If aggregate burnout is not complete in the oxidation region, then smoke is released to the surroundings in the fourth region where reactions cease but clusters continue to grow by CCA. The experiments yield the CCA growth rate within the flame which compares favorably with the theoretical value. The similarities and differences between this data reduction and the traditional analysis based on the use of cross sections for Rayleigh spheres and Mie theory spheres is discussed.

### NOMENCLATURE

$a_{i,j}$	function defined in Table 1	$d_{p,0}$	diameter of the primary particles as determined by optical observations
$b_{i,j}$	function defined in Table 1	$d_{p,i}$	diameter of the primary particles as determined by TEM observations
$c_{i,j}$	function defined in Table 1	$e$	2.718
$c_m$	mass of particles per unit volume	$E(m)$	function of $m$ defined by Eq. 14
$c_p$	function defined in Table 1	$f(x)$	function defined by Eqs. 7 and 8
$\overline{C_{sv}(\theta)}$	mean aggregate scattering cross section for a population of polydisperse aggregates, averaged over all orientations, when both incident light and scattered light are perpendicular to the plane of observation	$F(m)$	function of $m$ defined by Eq. 2
$D$	diameter of a spherical particle	$f$	the specific surface growth or oxidation rate of the primary particles defined by Eq. 23
$D_{30}$	volume weighted average of the volume equivalent diameters of a population of aggregates	$f_n$	the ratio $\overline{n^2}/(\overline{n^1})^2$
$D_f$	fractal dimension	$f_v$	volume of particles per unit volume
$d_{i,j}$	function defined in Table 1	$g(k^2 R_g^2)$	the function defined by Eq. 16
$d_p$	diameter of the primary particles	$I^A(\theta_i)$	normalized cross section for $sv$ differential scattering by a polydisperse aggregate population in random orientation
		$I_0$	power of the incident laser beam

$k$	wave number equal to $2\pi/\lambda$	$z$	vertical distance measured from the mouth of the burner
$k_B$	Boltzmann constant	$x_i$	$q_i^2 \overline{R_g^2}$
$k_f$	prefactor in the fractal power law, in Eq. A1	$x_p$	$\pi d_p/\lambda$
$K_a$	cluster-cluster aggregation rate	<b>Greek Symbols</b>	
$K_{\text{abs}}$	absorption coefficient of the aggregate population	$\lambda$	wavelength of light
$K_{\text{ext}}$	extinction coefficient of the aggregate population	$\theta_i, \theta_j$	scattering angles measured from the direction of propagation of the incident light
$L_{m,x}$	maximum dimension of an aggregate	$\bar{\kappa}$	function of $D_f$ , $k_f$ , and $p(n)$ defined by Eq. A3
$m$	complex refractive index	$\omega_p$	ratio of total scattering cross section to extinction cross section for primary particles
$n$	number of primary particles per aggregate	$\rho_p$	density of the primary particle material
$n_0$	minimum value of $n$ for a population of polydisperse aggregates	$\rho_{s,a}$	ratio of total scattering cross section to absorption cross section for a population of polydisperse aggregates
$n_g$	geometric mean of $n$ for a population of polydisperse aggregates	$\sigma_x$	geometric standard deviation used in Eq. A5
$n_x$	maximum value of $n$ for a population of polydisperse aggregates		
$\overline{n^q}$	$q$ th moment of the size probability function for a population of polydisperse aggregates		
$p(n)$	size distribution function for a population of polydisperse aggregates		
$N_a$	number of aggregates per unit volume		
$N_p$	number of primary particles per unit volume		
$q_i$	$2k \sin(\theta_i/2)$ , modulus of the scattering vector		
$Q_{w,i}(\theta_i)$	measured cross section for $w$ scattering per unit volume		
$r_{ij}$	the function defined in Table 1		
$R_g$	radius of gyration of an aggregate equal to the square root of the mean square distances from the center of mass of the aggregate to center of each primary particle		
$\overline{R_g^2}$	mean-square radius of gyration for a population of polydisperse aggregates as defined by Eq. 6		
$R_{ij}$	ratio of $Q_{w,i}(\theta_i)/Q_{w,j}(\theta_j)$		
$s_0$	normalization constant in Eq. A5		
$S_i$	surface area of aggregates per unit volume		
$t$	time		
$T$	temperature		
$v$	particle volume		

## INTRODUCTION

In a related earlier paper, the use of the optical cross sections for polydisperse aggregates was described to reduce the data from laser scattering/extinction tests conducted on the soot formed in a laminar diffusion flame using ethene as the fuel [1]. This development resulted from the recognition that the soot particles outside the inception region in the laminar ethene flame are found in the form of clusters of primary particles that possess a fractal-like character [2, 3]. These ideas, which were recognized in part in the earlier carbon black literature, have been formalized through the use of optical properties of mass fractals [4-6]. The optical cross sections for polydisperse aggregates composed of an absorbing material were subsequently formulated [7]. The present work takes advantage of an improved experimental arrangement wherein the intensity of the scattered laser light was measured simultaneously at three angles  $\theta_i$ —45°, 90°, and 135°. Line-of-sight extinction measure-

ments were obtained separately from the simultaneous angular scattering measurements and reduced to point measurements by a tomographic inversion procedure [8].

The simultaneous observation of the angular distribution of scattered light results in an improved data set over that obtained by the sequential data acquisition approach previously used [1]. Using the present approach, ratios of the scattered light measurements at various angles are less affected by small variations due to changes in the flame conditions (e.g., flame movement) since angular dissymmetry information is constructed from data taken simultaneously at each angle. Using these improved data, a more detailed analysis of the optical observations is described herein. This approach allows an iterative analysis to determine the fractal dimension rather than imposing a value for this quantity based on work by other investigators, as was done previously [1]. Additionally, new information of the prefactor,  $k_f$ , in the fractal power law analysis has been incorporated into the present work. These developments allow new information to be derived on the surface growth and oxidation rates observed in these flames and to further refine the treatment of the aggregation process. A clearer relationship between the number of aggregates per unit volume and the number of primary particles per unit volume is also observed. From these observations we arrive at a global description of physical processes associated with the formation, growth, and oxidation of the soot aggregates formed in a laminar ethene diffusion flame.

The data reduction performed herein is based on the optical cross sections that have been formulated for polydisperse aggregates that apply over a wide range of size parameters, widths of distribution functions, and refractive indices for absorbing or dielectric particles [7]. The differential and total scattering cross sections are a generalization of the numerical simulations of aggregates formed by Langevin mechanics [9]. The aggregates found in the latter study comply with the power law for mass fractals even when the number of primary particles per aggregate are as small as  $O(10)$ . Such aggregates are too small to display the scale similarity property of mass fractals,

and they are said to be "fractal-like." Optical absorption cross sections of aggregates were based on the results of various investigators who have found them to be well approximated by the volume absorption of the component primary particles.

#### EXPERIMENTAL APPARATUS AND DATA ACQUISITION

The coannular burner used in these experiments consists of an inner tube of 11.1 mm i.d., which is supplied with c.p. grade ethene at a flow rate of  $3.85 \text{ cm}^3/\text{s}$ . A coannular air stream is provided through a ceramic honeycomb grid filling the intervening air region which has a 101.6 mm i.d. The air stream flow rate is  $713 \text{ cm}^3/\text{s}$  and is guided by a metal chimney with slots that permit the passage of a laser beam and the observation of the light scattering that it produces. A detailed description of this coannular burner is given elsewhere [10]. With ethene as a fuel, the resulting flame height is about 88 mm, and the soot formed within the flame is fully oxidized within the flame.

The apparatus used to measure the laser extinction and scattering signals from soot particles in the flame utilized a 4-W argon ion laser operating at the 514.5-nm laser line. The incidence power,  $I_0$ , was 0.5 W and was modulated using a mechanical chopper operating at 1015 Hz. The incident beam was passed through a polarization rotator that allowed adjustment of the polarization orientation. For these experiments all measurements were obtained for vertically polarized light having a polarization ratio of better than 400:1.

The beam was focused into the burner region with a 400-mm focal length lens, which resulted in a beam whose diameter was approximately 0.2 mm. The transmitted power,  $I$ , was measured using a silicon photodiode after attenuation by neutral density filters (N.D.  $\approx 2.0$ ) to reduce the beam intensity to acceptable levels. Scattered light receivers were located at angles  $45^\circ$ ,  $90^\circ$ , and  $135^\circ$  with respect to the forward propagation direction of the incident beam. Each of the scattered light receivers consisted of a polarizer, circular aperture, collection lens, pinhole aperture, laser line filter

for 514.5 nm ( $\Delta\lambda = 1$  nm) and a Hamamatsu R928 photomultiplier tube. A circular aperture (12.7 mm diameter) defined the scattered light collection solid angle to be  $1.2 \times 10^{-3}$  sr. A pinhole aperture (1 mm diameter) defined the length of the sample volume to be 1 mm since the optical system was set up to have unity magnification. The polarizers had rejection ratios of  $1 \times 10^{-4}$ .

Each of the scattered light detectors was connected to a lock-in amplifier that was operated with a time constant of 0.30 s. Data acquisition from the lock-in amplifiers using an IBM-XT personal computer employing a GPIB interface provided for near-simultaneous data acquisition from each detector. Consequently, the resulting dissymmetry measurements formed from the ratio of the detector signals were not subject to problems resulting from small changes in the probe volume location due to flame movement over the period of the measurement. The time between acquisition of sequential measurements from the individual lock-in amplifiers was determined to be less than 100  $\mu$ s. This procedure resulted in improved angular dissymmetry measurements as compared with previously reported results [1]. Separate runs were used to measure the dissymmetry ratio and the extinction measurements since only three lock-in amplifiers were available. However, previous work has shown that the present laminar diffusion flame apparatus produced highly reproducible measurement conditions.

The scattered light detection systems were calibrated using a Rayleigh scattering technique previously described [10]. This approach accounts for the effects of the incident laser power, sample volume, light collection efficiency, photomultiplier sensitivity, and electronic gain of the system.

Radial profiles of light scattering and extinction measurements were obtained at fixed axial locations in the flame ( $Z = 10, 15, 20, 30, 50, 60,$  and  $70$  mm). The local soot extinction (and subsequently, the soot volume fraction) were obtained from the extinction measurements using a tomographic inversion procedure [8], while the ratio of the scattered light signals,  $R_{ij}$ , was calculated directly after accounting for the detection system calibrations. The data

analysis was carried out for soot aggregates that were formed along the particle path possessing the maximum soot volume fraction.

The information on the particle path, which is needed to relate the measurements made at different flame locations, was achieved using measurements of the velocity field in the flame. These velocity measurements were obtained using a single component laser velocimeter. Sequential profiles were obtained to provide information on both the radial and axial components of the velocity field. These measurements were then used to construct the appropriate particle path possessing the maximum soot volume fraction in the flame [11].

#### DATA ANALYSIS

The data analysis uses the cross sections [7] that were previously employed [1] in a more advantageous procedure that no longer requires an assumed value of the fractal dimension  $D_f$  because of the improved quality of the angular scattering data as discussed previously. The normalized cross section for  $vv$  differential scattering (i.e., vertically polarized scattered light produced by vertically polarized incident light) by a polydisperse aggregate population in random orientation is defined by

$$\overline{I^A(\theta_i)} = \frac{k^2 \overline{C_{vv}(\theta_i)}}{x_p^6 F(m)} \quad (1)$$

where  $\overline{C_{vv}(\theta_i)}$  is the population-averaged differential scattering cross section,  $k$  is the wavenumber equal to  $2\pi/\lambda$ , where  $\lambda$  is the wavelength of light, and  $x_p$  is  $\pi d_p/\lambda$ , where  $d_p$  is the diameter of the primary particles. The volumetric scattering cross section,  $Q_{vv}(\theta_i)$ ,  $\text{cm}^{-1} \text{sr}^{-1}$ , which is directly measured through a calibration procedure described elsewhere [10], is the product of the scattering cross section  $\overline{C_{vv}(\theta_i)}$  ( $\text{cm}^2$ ), and the aggregate number concentration  $N_a$  ( $\text{cm}^{-3}$ ). The quantity  $F(m)$  is given by

$$F(m) = \left| \frac{m^2 - 1}{m^2 + 2} \right|^2 \quad (2)$$

where  $m$  is the complex refractive index of the soot particulate material. Several moments of

the aggregate probability distribution function (pdf) enter into the relations for the optical cross sections. The  $q$ th moment of the pdf is defined by

$$\bar{n}^q = \sum_n n^q p(n). \quad (3)$$

Here the discrete function  $p(n)$  is defined such that  $\sum p(n)$  over the interval  $n_1$  to  $n_2$  represents the fraction of the population having more than  $n_1$  and less than  $n_2$  primary particles per aggregate. The first moment  $\bar{n}^1$  is the average number of primary particles per aggregate. The moment ratio  $f_n$  is defined by

$$f_n = \bar{n}^2 / (\bar{n}^1)^2 \quad (4)$$

and can be used to relate  $\bar{n}^2$  to  $\bar{n}^1$ . While limited information is available on  $p(n)$ , reasonable estimates of moment ratios such as  $f_n$  can be made as discussed in the Appendix. Each aggregate has a volume-equivalent diameter  $D = n^{1/3} d_p$ , and the volume-weighted average diameter of the volume-equivalent spheres,  $D_{30} = (\bar{n}^1)^{1/3} d_p$ , is an important quantity that appears in the equations given below [3].

The quantity  $I^A(\theta)$  divided by  $\bar{n}^2$  is a function only of the quantity  $x_i = q_i^2 R_g^2$ , where  $q_i$ , the modulus of the scattering vector, is given by

$$q_i = 2k \sin(\theta_i/2). \quad (5)$$

and the mean-square radius of gyration is defined by

$$\overline{R_g^2} = \frac{\sum_n R_g^2(n) n^2 p(n)}{\sum_n n^2 p(n)}. \quad (6)$$

Thus for  $0 < x_i < 1.5D_f$  where  $D_f$  is the fractal dimension,  $f(x_i)$  is given by the Guinier law

$$\frac{I^A(\theta_i)}{\bar{n}^2} = f(x_i) = \exp(-x_i/3). \quad (7)$$

This expression was originally presented as an approximate relationship for scattering of x-rays by an electron cloud, and is also applica-

ble to aggregates [5]. Recently Eq. 7 has been found to provide a good description of differential scattering for populations of polydisperse aggregates irrespective of the width of distribution function [7] when the mean-square radius of gyration defined by Eq. 6 is employed.

For  $x_i \ll 1$ ,  $f(x_i) \rightarrow 1$  and the differential scattering cross sections of an aggregate is the same as for a sphere of equal volume. To a good approximation in this instance both the  $w$  scattering cross section and the absorption cross section depend only upon the volume of the material irrespective of the particle shape. Thus a small sphere and a small aggregate of equal volume behave identically in both  $w$  scattering and extinction, and observations of these cross sections provide no information on which of these two disparate morphologies is actually present. For most of the observations reported below, the aggregates were large enough so that  $x_i \approx 1$  or larger.

When  $x_i > 1.5D_f$ , the power law form for  $f(x_i)$  is applicable:

$$f(x_i) = \left( \frac{1.5D_f}{ex_i} \right)^{D_f/2}, \quad (8)$$

where  $e = 2.718$ .

For two angles with  $x_i$  and  $x_j$  both  $\leq 1.5D_f$ , it follows that the measured cross sections at two angles can be used to determine the mean-square radius of gyration without a knowledge of refractive index or any information on the size distribution function. From Eqs. 1 and 7 we find

$$\overline{R_g^2} = \frac{a_{ij}}{k^2} \ln(R_{ij}), \quad (9)$$

where  $R_{ij} = Q_{wv}(\theta_j)/Q_{wv}(\theta_i)$  and  $a_{ij}$  is a constant (Table 1) for given angles and  $1 < R_{ij} \leq$

TABLE I

Equations for the Constants Used in Determination of the Mean-Square Radius of Gyration Using Eqs. 9 or 10.

$r_{ij} = \sin(\theta_i/2)/\sin(\theta_j/2)$	$a_{ij} = 0.75 \left[ \sin^2\left(\frac{\theta_i}{2}\right) - \sin^2\left(\frac{\theta_j}{2}\right) \right]$
$b_{ij} = \exp[0.5 D_f(1 - r_{ij}^2)]$	$c_{ij} = (r_{ij})^{-D_f}$
$d_{ij} = c_{ij}/C_p$	$C_p = (1.5 D_f/e)^{D_f/2}$

$b_{ij}$ . When  $\theta_j(\theta_j > \theta_i)$  is such that  $q_j^2 \overline{R_g^2}$  is greater than  $1.5D_f$  (corresponding to  $b_{ij} < R_{ij} < c_{ij}$ ), both Eqs. 7 and 8 must be employed and a transcendental equation for  $x_i$  results:

$$x_i \exp\left(\frac{-x_i}{1.5D_f}\right) = \left(\frac{R_{ij}}{d_{ij}}\right)^{2/D_f} \quad (10)$$

The equations for the quantities  $a_{ij}$ ,  $b_{ij}$ ,  $c_{ij}$ , and  $d_{ij}$ , which are given in Table 1, depend upon the angles selected and, with one exception ( $a_{ij}$ ), also depend upon  $D_f$ . From Eq. 8 it follows that the slope of the curve of  $\log(I^A/\overline{n^2})$  versus  $\log x_i$  is equal to  $-D_f/2$ . This property has been widely used to infer the fractal dimension of populations of aggregate structures (e.g., Ref. 4).

The extinction coefficient for a polydisperse population of aggregates is the sum of the absorption coefficient and the total scattering coefficient [7]; also see Appendix II of Ref. 1. It can be expressed as

$$K_{\text{ext}} = K_{\text{abs}}(1.0 + \rho_{sa}), \quad (11)$$

where  $K_{\text{abs}}$  is given by

$$K_{\text{abs}} = \frac{4\pi N_a \overline{n^3} x_p^3 E(m)}{k^2}, \quad (12)$$

and  $\rho_{sa}$ , the ratio of scattering to absorption, is given by

$$\rho_{sa} = \omega_p f_n \overline{n^1} g(k^2 \overline{R_g^2}) \quad (13)$$

and  $E(m)$  is given by

$$E(m) = -\text{Im}\left(\frac{m^2 - 1}{m^2 + 2}\right). \quad (14)$$

Here  $\omega_p$  is the albedo of the primary particle and is given by

$$\omega_p = \frac{2}{3} x_p^3 \frac{F(m)}{E(m)} \quad (15)$$

and

$$g(k^2 \overline{R_g^2}) = \left(1 + \frac{4}{3D_f} k^2 \overline{R_g^2}\right)^{-D_f/2} \quad (16)$$

The functions of  $f(x_i)$  and  $g(k^2 \overline{R_g^2})$  determine the departure of the scattering cross sections from the Rayleigh values that are applicable for small aggregates. The soot volume fraction is related to the aggregate average volume and number concentration by

$$f_v = \frac{\pi d_p^3 \overline{n^1} N_a}{6}, \quad (17)$$

and, in view of the Eq. 12 for the volumetric absorption, the volume fraction can be expressed as

$$f_v = \frac{K_{\text{abs}}}{3kE(m)}. \quad (18)$$

The volumetric  $vw$  scattering cross section is the product of the corresponding mean cross section and the aggregate number concentration  $N_a$  and is given by

$$Q_{vw}(\theta_i) = \frac{f_n(\overline{n^1})^2 x_p^6 F(m) N_a f(x_i)}{k^2}. \quad (19)$$

Specifying  $\theta_2 = 90^\circ$  in the above expression, dividing by  $K_{\text{abs}}$ , and noting that  $\overline{n^1} d_p^3 = D_{30}^3$ , we find

$$D_{30} = \left(\frac{\lambda}{\pi}\right) \left(\frac{4\pi E(m) Q_{vw}(\theta_2)}{f_n F(m) f(x_2) K_{\text{abs}}}\right)^{1/3}. \quad (20)$$

The aggregate number concentration  $N_a$  is given by

$$N_a = \frac{f_v}{\frac{\pi}{6} D_{30}^3}. \quad (21)$$

The fractal power law for polydisperse aggregates that is discussed further in the Appendix leads to [3]

$$d_{p0} = \frac{D_{30}^3}{\overline{\kappa} R_g^2}. \quad (22)$$

From Eqs. 20 and 22 it is apparent that  $d_{p0}$  is inversely proportional to the quantity  $[\overline{\kappa} f_n F(m)/E(m)]$  and is clearly sensitive to

both the aggregate pdf through the product  $\bar{k}f_n$  and the refractive index  $m$  through the quotient  $F(m)/E(m)$ . Thus uncertainties in either the aggregate pdf or the refractive index propagate into the determination of the primary particle size  $d_{p0}$  yielded by Eq. 22.

The data reduction proceeds as described below using the optical observations and TEM data reported in Table 2. The values of  $\overline{R_g^2}$  are first found using Eq. 9 or 10 with an estimated value of  $D_f$ . The values of the primary particle diameters  $d_{p1}$  determined from the TEM observations [12] are used with  $\overline{R_g^2}$  to find  $\bar{n}_1$  from Eq. A2 with estimated values of  $\bar{k}$  and  $f_n$  (see below),  $g(kR_g^2)$  from Eq. 16,  $\rho_{va}$  from Eq. 13,  $K_{abs}$  from  $\rho_{va}$  and the measured  $K_{ext}$ , and  $D_{30}$  from Eq. 20. The quantity  $\overline{I^A(\theta_i)/n^2}$  is then calculated and, when  $q^2\overline{R_g^2} > 1.5D_f$ , is used to determine the value of the fractal dimension  $D_f$  and the full calculation is reiterated. Finally the values of the number concentration of aggregates  $N_a$  and the optically determined primary particle size  $d_{p0}$  are found.

In these experiments, individual measurements for light scattering and extinction were averaged in over 100 observations. For the scattering measurements ( $Q_{sc}$ ) at heights  $z$  of 15, 20, and 70 mm, fluctuations owing to noise on the signal amounted to a probable error of  $\pm 10\%$ , which we estimated to be the uncertainty of these quantities. At intermediate heights ( $z = 30, 50,$  and  $60$  mm), the observed

noise amounted to  $\pm 2\%$ . On the other hand, the observations at the lowest measured height ( $z = 10$  mm) displayed  $\pm 20\%$  fluctuations. Similar analysis for the extinction measurements yielded an estimated noise error of  $\pm 1\%$ . However, based on experience with repeated extinction measurements, the local extinction values are estimated to have an error of  $\pm 10\%$ . This error is largely due to slight asymmetries in the radial extinction profiles which are reflected in the subsequent tomographic inversion analysis.

Based on these considerations, the probable uncertainty in  $f_n$  at intermediate heights is estimated as  $\pm 15\%$ . The quantities  $R_g$  and  $D_{30}$  are believed to have similar uncertainties. In our procedure, TEM data on  $d_{p1}$  is used for which small uncertainties are achieved ( $\pm 10\%$ ). The quantities  $N_a$ ,  $S_1$ , and  $n^1$  have the greatest uncertainty ( $\pm 50\%$ ) that is aggravated in the case of the lowest height. The information conveyed in the figures given below should be viewed with this discussion in mind.

Uncertainties are also present in this calculation relating to the refractive index and the aggregate size pdf, which, in the data reduction procedure is characterized by the product  $f_n\bar{k}$ . In the present calculation we use trial values of  $f_n\bar{k}$  to find the best agreement between the values of  $d_{p0}$  yielded by Eq. 22 and the values  $d_{p1}$  yielded by TEM observations. As an objective procedure, we select the value of  $f_n\bar{k} = (f_n\bar{k})_{min}$  that yields the smallest fractional rms value of  $[d_{p0} - d_{p1}]$  summed over all values of  $z$  for a given refractive index.

The three values of refractive index, which span the range of the numerous values applicable to soot that are quoted in the literature, have been employed in reducing the data and are listed in Table 3 along with the corresponding values of  $(f_n\bar{k})_{min}$ . Of the several results given in Table 3, the value of  $m = 1.90 - i0.55$  provides the most reasonable values of  $f_n\bar{k} = 5.5$  and for the aggregation rate  $K_a$ , as discussed below. This value of  $f_n\bar{k}$  corresponds to aggregate pdfs of intermediate widths, as described in the Appendix. (In estimating  $\bar{k}$  and thus  $f_n\bar{k}$  we employ a prefactor  $k_f$  appearing in the fractal power law equal to 9.0 that is based on experimental observations for soot particles; see the Appendix).

TABLE 2

Optical Observations and Other Input Data on the Laminar, Nonsmoking Ethene Flame ( $3.85 \text{ cm}^2/\text{s}$ )

Z (mm)	$t^a$ (ms)	$K_{ext}$ ( $\text{cm}^{-1}$ )	$Q_{sc}(\theta_z)$ ( $\text{cm}^{-1} \text{sr}^{-1}$ )	$R_{12}$	$R_{13}$	$d_{p1}^b$ (nm)
10.	25.1	0.0657	4.68E-5	1.109	1.150	13
15.	31.3	0.235	1.58E-3	1.250	1.432	22
20.	36.1	0.443	5.47E-3	1.658	2.225	27
30.	44.1	0.836	1.54E-2	2.138	3.380	32
50.	56.4	0.828	1.38E-2	2.883	4.237	32
60.	61.4	0.459	6.21E-3	2.677	4.255	27
70.	66.5	0.0781	6.41E-4	2.037	2.402	19

<sup>a</sup>Derived from laser doppler anemometry observations [11].

<sup>b</sup>From thermophoretic sampling and TEM observations [12].

TABLE 3  
Values of  $(f_n \bar{\kappa})_{\min}$  and  $K_a$  for Selected Values of Refractive Index

$m$	Ref.	$F(m)/E(m)$	$(f_n \bar{\kappa})_{\min}$	$K_a (\text{cm}^3/\text{s})$
1.57 - $i0.56$	Dalzell and Sarofim [13]	0.837	10.1	$236 \times 10^{-10}$
1.90 - $i0.55$	Lee and Tien [14]	1.55	5.50	$95 \times 10^{-10}$
2.10 - $i0.55$	Vaglieco et al. [15]	2.16	3.92	$57 \times 10^{-10}$

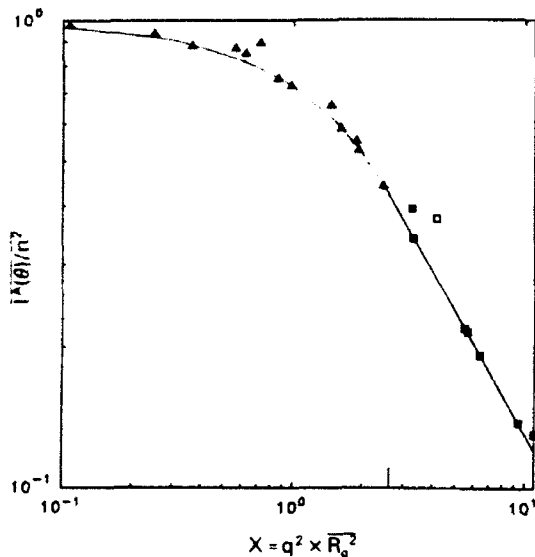


Fig. 1. Normalized intensity  $I^A(\theta)/n^2$  versus  $q^2 R_g^2$ . The slope of the regression line for  $q^2 R_g^2 > 1.5D_f$  (solid squares) yields  $D_f$  of 1.74. See discussion in text.

## DISCUSSION OF RESULTS

The graph of  $I^A(\theta)/n^2$  versus  $x$ , is shown in Fig. 1 using the observed volumetric cross sections and reduced values of  $N_a$ ,  $d_{pr}$ ,  $n^1$ , and  $R_g^2$  to find the ordinate and the abscissa. The seven data points (solid squares) to the right in Fig. 1 lie in the power law regime where Eq. 8 is applicable. [One point, an open square, at the top of the flame where rapid burnout is in progress correlated poorly and was not used in the determination of  $D_f$ .] The slope of the least square straight line through these points yields a fractal dimension of 1.74. The smooth curve in Fig. 1 is the theoretical curve for the dimensionless cross section given by Eqs. 7 and 8 for a fractal dimension  $D_f = 1.74$ . The curvature of a mean line through the data points corresponds well to that of the theoretical curve, and the experimental points show the

transition from Rayleigh scattering ( $x \ll 1$ ), to Guinier regime ( $x \approx 1$ ), and to the power law regimes.

The value  $D_f = 1.74$  is in general agreement with the results of several experimental observations of soot aggregates in flames that fall within the range of 1.5–1.8 (see Table 4). These results are generally only slightly lower than the values, 1.7–1.9, that typically are found in numerous computer simulations of free molecular (ballistic) CCA. Noteworthy is the fact that the fractal dimension of the aggregation process in the flame, where primary particle growth and contraction occur successively, agrees with the computer simulations that use a constant primary particle diameter. This suggests, if only preliminarily, that the growth and oxidation processes do not significantly alter the fractal dimension of the aggregates formed in their presence.

The quantities  $f_n$ ,  $d_{pr}$ , and  $D_{30}$  are plotted versus time in Fig. 2. These three curves show maximum values at about 56 ms, which corresponds to a height  $z = 50$  mm. This point in the flame marks the transition from the growth region, where surface growth and CCA are cooperative, to the oxidation region where oxidation reactions oppose surface growth.

In Fig. 3 the number concentrations of the aggregates and primary particles  $N_a$  and  $N_p$  are plotted versus time. These values are consistent with the sustained action of CCA tending to increase aggregate size throughout the growth region and even into the oxidation region. The number concentration of the primary particles remains constant except at early and late times. The gas temperature and density remain essentially constant along the particle path of maximum soot concentration which, in the lower portion of the flame, lies within the high temperature flame front. The early time behavior is consistent with the possibility that some coagulation occurs at the beginning

TABLE 4

Summary of Experimental Determination of  $D_f$  for Soot Aggregates in Flames by Various Investigators

Investigators	Fuel and Flame Type	Method	$D_f$
Sampson, et al. [16]	C <sub>2</sub> H <sub>2</sub> Diffusion Flame (Sample from smoke plume above flame)	TEM Observation	1.5 to 1.6
Zhang et al. [17]	CH <sub>4</sub> /O <sub>2</sub> Premixed (Sample extracted to Optical cell)	Light Scattering, TEM	1.61 ± 0.06, 1.72 ± 0.10
Megaridis and Dobbins [3]	C <sub>2</sub> H <sub>4</sub> Diffusion Flame	TEM Observation	1.62 ± 0.04 1.74 ± 0.06
Gangopadhyay et al. [18]	CH <sub>4</sub> /O <sub>2</sub> Premixed Flame	In Situ Light Scattering	1.6 to 1.8
Charalampopoulos and Chang [19]	C <sub>3</sub> H <sub>8</sub> /O <sub>2</sub> Premixed	In Situ Light Scattering	1.7 ± 0.08
Sorensen et al. [20]	CH <sub>4</sub> /O <sub>2</sub> Premixed	In Situ Light Scattering	1.70 to 1.75
Present study	C <sub>2</sub> H <sub>4</sub> Diffusion Flame	In Situ Light Scattering with TEM	1.74 ± 0.1

of the region where surface growth is prominent.

The particle surface area and specific growth/oxidation rate are presented in Fig. 4. The latter is given by

$$f = \pm \frac{1}{S_t} \frac{dc_m}{dt} = \pm \frac{\rho_p}{S_t} \frac{df_v}{dt} \quad (23)$$

where  $c_m$  is the particle mass per unit volume,  $S_t$  is the particle surface per unit volume, and  $\rho_p$  is the particle material density, which is taken to be 1.86 g/cm<sup>3</sup>. The plus sign refers to the specific growth rate and the minus sign to the specific oxidation rate. The derivative in Eq. 23 was evaluated by differentiating a least-squares-fit to a third order polynomial.

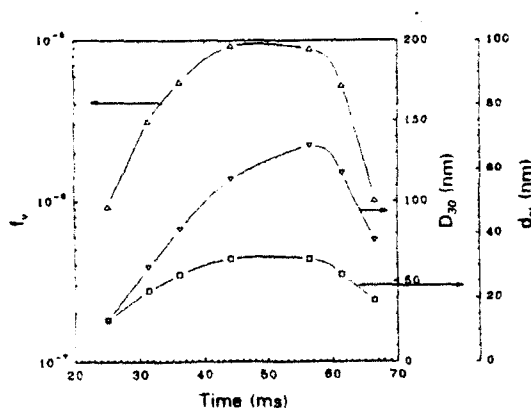


Fig. 2. Volume fraction  $f_v$ , primary particle diameter (from TEM)  $d_p$ , and volume mean diameter  $D_{30}$  versus time.

The maximum specific growth rate shown in Fig. 4,  $15 \times 10^{-5}$  g/cm<sup>2</sup>/s, is somewhat higher than previously reported for this flame [12] using a less detailed data reduction. This value is close to the maximum value reported for a premixed ethene flame [21]. The growth rate of the primary particles decreases as oxidation becomes dominant above the midflame height. The oxidation rate rises very rapidly as the aggregates approach the high-temperature envelope, which surrounds the soot-bearing luminous region and which is rich in the oxidizing OH and O<sub>2</sub> species. The oxidation rate

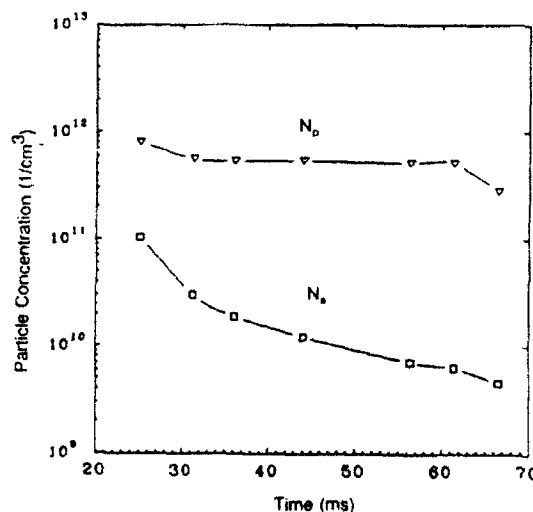


Fig. 3. Number concentration of primary particles  $N_p$  and of aggregates  $N_a$  versus time.

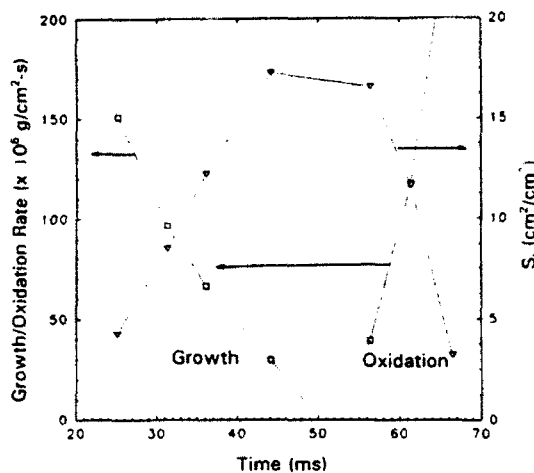


Fig. 4. Growth/oxidation rates,  $f$ , and surface area,  $S_p$ , versus time.

continues beyond  $7.5 \times 10^{-4}$  g/cm<sup>2</sup>/s, which is measured at  $z = 70$  mm. The specific oxidation rate that is reported for a methane diffusion flame ranges up to about  $10^{-3}$  g/cm<sup>2</sup>/s [22].

Figure 5 is a graph of the mean-square radius of gyration  $R_g^2$ , the primary particle diameter as determined by TEM  $d_{pt}$ , and the average number of primary particles per aggregate  $n^1$ . Both  $R_g^2$  and  $n^1$  reach peak values later than  $d_{pt}$ , apparently because cluster-cluster aggregation continues in progress after oxidation of the primary particles commences. High-resolution probing of the soot burnout region of the flame would be required to determine if

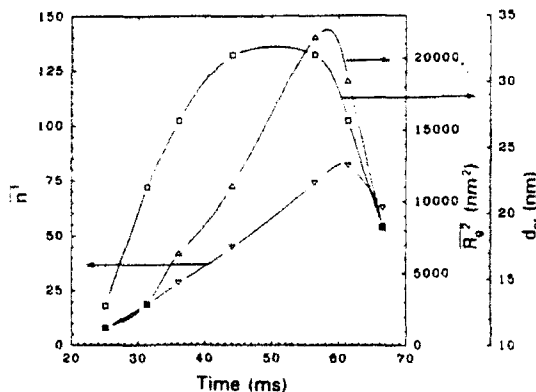


Fig. 5. Mean-square radius of gyration  $R_g^2$ , average number of primary particles per aggregate  $n^1$ , and primary particle diameter from TEM  $d_{pt}$ , versus time.

Determination of Aggregation Rate

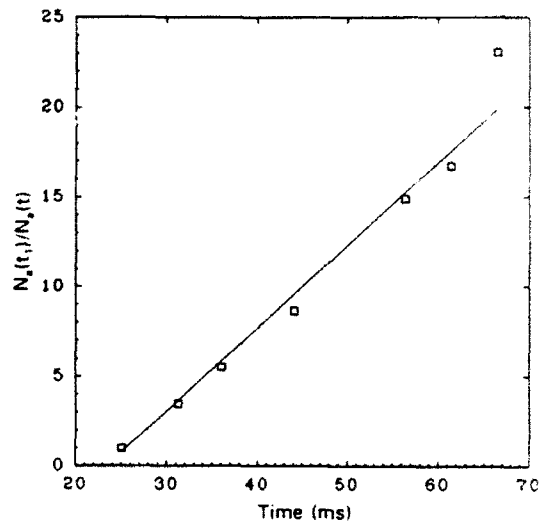


Fig. 6.  $N_a(t_1)/N_a(t)$  versus time. The slope of the least-square straight line yields the cluster-cluster aggregation rate equal to  $95 \times 10^{-10}$  cm<sup>3</sup>/s.

these maxima are an indication of aggregate breakup as a result of oxidation.

The disappearance of aggregates occurs through CCA and the aggregation rate is yielded by the first moment of the aerosol dynamic equation in the absence of particle generation. Provided the particle collision rate is not strongly size dependent, the result is

$$\frac{dN_a}{dt} = -\frac{1}{2}K_a N_a^2 \quad (24)$$

This equation can be rearranged as

$$K_a = \frac{2}{N_a(t_1)} \frac{d}{dt} \left( \frac{N_a(t_1)}{N_a(t)} \right) \quad (25)$$

In Fig. 6 we present a graph of the ratio  $N_a(t_1)/N_a(t)$ , whose slope is the CCA aggregation rate which shows a linear behavior except at late times when aggregate burnout is in progress. From Fig. 6, which is based on  $m = 1.90 - i0.55$ , we find a CCA rate of  $95 \times 10^{-10}$  cm<sup>3</sup>/s.

The theoretical coagulation rate  $K_a$  for spherical particles small compared with the

molecular mean free path is

$$K_a = \left(\frac{3}{4\pi}\right)^{1/6} \left(\frac{6k_B T}{\rho_p}\right)^{1/2} (v_1^{1/3} + v_2^{1/3})^2 \times \left(\frac{1}{v_1} + \frac{1}{v_2}\right)^{1/2} \quad (26)$$

where  $k_B$  is the Boltzman constant,  $\rho_p$  is the particle density,  $T$  is the gas temperature, and  $v_1$  and  $v_2$  are the particle volumes. For two colliding spheres of equal diameter  $D$  this equation reduces to

$$K_a = 4 \left(\frac{6Dk_B T}{\rho_p}\right)^{1/2} \quad (27)$$

For a size  $D$  of 100 nm when  $T = 1700$  K we find a theoretical value of  $K_a$  equal to  $110 \times 10^{-10}$  cm<sup>3</sup>/s. The use of twice the mean-square radius of gyration in lieu of the particle diameter does not significantly change this rate, which varies as the square root of the particle length scale. The agreement between the observed aggregation rate and the theoretical coagulation rate is reasonable.

#### COMPARISON WITH DATA REDUCTION BASED ON RAYLEIGH AND MIE THEORIES FOR SPHERES

The data reduction based on aggregate cross sections shows significant differences from those employing Mie and Rayleigh cross sections for spheres. The volume mean diameter that is yielded in the case of the Mie and Rayleigh data reduction shows a much more moderate increase in the growth region and a very modest decrease throughout the oxidation region even though soot volume fraction is found to decrease dramatically. In the Rayleigh sphere data reduction, the particle number concentration tends to increase slightly throughout the growth region where CCA actually would be expected to cause  $N_p$  to decrease. In the Mie data reduction, the volume mean diameter can be calculated by one of two methods—from scattering/extinction ratio or from dissymmetry measurements. Of these two

methods, the latter gives a larger volume mean diameter and smaller surface area per unit volume, and these self-contradictory results immediately call into question the applicability of Mie theory. The particle number concentration obtained from the Mie data reduction using scattering/extinction cross sections is invariant along most of the streamline. This implies the absence of CCA or that CCA is offset by an increase in the aggregate population through inception. Additionally, the Mie data reduction using dissymmetry measurements gives a much lower number concentration which decreases monotonically. This analysis also seems unreasonable since it yields more than twice the theoretical aggregation rate. The peak soot volume fraction is about 30% higher for Rayleigh and about 15% lower for Mie sphere data reduction at the intermediate heights where the aggregates are largest. Thus, while the Rayleigh data reduction ignores any contribution of scattering to extinction, the Mie data reduction appears to overestimate this contribution compared to the aggregate data reduction. Finally, the Rayleigh data reduction predicts a surface area per unit volume that is lower than the prediction aggregate theory by a factor of about two. The Mie theory prediction of this quantity is lower by a factor of 3–6 depending on the method by which the volume mean diameter is employed. These predictions are considered unrealistic in view of the well documented aggregate structure of the particles in this flame.

#### SUMMARY

The data reduction of the soot particle field that is based on the presence of aggregate morphology presents an internally consistent picture of the development of the soot particle field in the laminar ethene flame. This is summarized in Fig. 7, where the regions within this flame corresponding to the various processes are depicted.

Low in the flame there is an annular region of particle inception where preparticle chemical reactions produce a high concentration of primary particles which solidify and collide to form young aggregates. Detailed observations within the inception region are difficult because

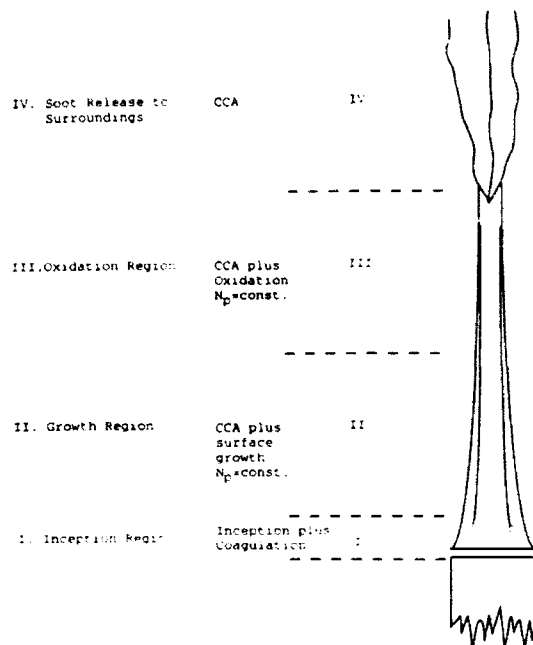


Fig. 7. A schematic representation of the soot aerosol dynamic processes in the laminar ethene diffusion flame.

of the rapid rates and high spatial gradients. The primary particle concentration that is established in the inception region remains unchanged along the soot particle path of maximum soot concentration throughout the flame until the particles are totally oxidized or, alternatively, released to the surroundings after partial oxidation.

Above the inception zone is the growth region where the primary particles grow from 10 to about 35 nm by surface growth, and CCA simultaneously causes cluster growth. The values of  $d_p$ ,  $D_{30}$ ,  $R_g^2$ , and  $n^1$  increase while the primary particle concentration  $N_p$  remains constant.

The upper portion of the flame is an oxidation region wherein primary particles contract due to oxidation reactions. The size-related quantities  $d_p$ ,  $D_{30}$ , and  $f_v$  decrease but again the primary particle number concentration remains relatively constant. Complete particle burnout occurs in this region in the case of the nonsmoking flame whose flame height is less than the smoke point height. Taller flames release smoke to the surroundings in the fourth region where chemical reactions cease to be important but CCA can continue to be present.

The aggregate data reduction of the scattering/ extinction measurements yields values of the fractal dimension that are in agreement with the value found by TEM for this same diffusion flame [3] as well as with in situ observations on various hydrocarbon flames (Table 4). The rate of aggregation of the clusters is found to be in general agreement with coagulation theory. The particle surface areas per unit volume are considered to be more reliably measured and these are expected to provide improved values of the soot specific growth and oxidation rates. Finally, only the aggregate data reduction yields a satisfactory description of the evolution of the soot aerosol and the regional partitioning of the soot aerosol dynamic processes within this flame.

*This research was performed under the sponsorship of the U.S. Department of Commerce, National Institute of Standards and Technology, Center for Fire Research under grant number 60NANB01035 to the Pennsylvania State University and grant numbers 60NANB9D0975 and 60NANB1D1110 to Brown University. Two of the authors (RJS and TFR) would also like to acknowledge support by the Air Force Office of Scientific Research under Award No. AFOSR-87-0145. One author (RAD) was supported in part by the Army Research Office under Grant No. DAAL03-92-G-0023.*

## REFERENCES

1. Dobbins, R. A., Santoro, R. J., and Semerjian, H. G., *Twenty-Third Symposium (International) on Combustion*, The Combustion Institute, Pittsburgh, 1990, p. 1525.
2. Dobbins, R. A., and Megaridis, C. M., *Langmuir* 3:254-259 (1987).
3. Megaridis, C. M., and Dobbins, R. A., *Combust. Sci. Technol.* 71:95-109 (1990).
4. Schaefer, D. W., Martin, J. E., Wiltzius, P., and Cannel, D. S., *Phys. Rev. Lett.* 52:2371-2374 (1984).
5. Jullien, R., and Botet, R., *Aggregation and Fractal Aggregates*, World Scientific, Singapore, 1987, p. 46.
6. Botet, R., and Jullien, R., *Ann. Phys. Fr.* 13:153-221 (1988).
7. Dobbins, R. A., and Megaridis, C. M., *Appl. Optics* 30:4747-4754 (1991).
8. Semerjian, H. G., Santoro, R. J., Goulard, R., and Emmerman, P. J., in *Fluid Mechanics of Combustion Systems* (T. Morel, R. P. Lohmann, and J. M. Rackley,

- Eds.), American Society of Mechanical Engineers, New York, 1981, p. 119.
9. Mountain, R. D., and Mulholland, G. W., *Langmuir* 4:1321-1326 (1988).
  10. Santoro, R. J., Semerjian, H. G., and Dobbins, R. A., *Combust. Flame* 51:203-218 (1983).
  11. Santoro, R. J., Yeh, T. T., Horvath, J. J., and Semerjian, H. G., *Combust. Sci. Technol.* 53:89-115 (1987).
  12. Megaridis, C. M., and Dobbins, R. A., *Combust. Sci. Technol.* 66:1-16 (1989).
  13. Dalzell, W. H., and Sarofim, A. F., *J. Heat Transf.* 91:100-104 (1969).
  14. Lee, S. C., and Tien, C. L., *Eighteenth Symposium (International) on Combustion*, The Combustion Institute, Pittsburgh, 1981, p. 1159.
  15. Vaglieco, B. M., Baretta, F., and D'Alessio, A., *Combust. Flame* 79:259-271 (1990).
  16. Sampson, R. J., Mulholland, G. W., and Gentry, J. W., *Langmuir* 3:272-281 (1987).
  17. Zhang, H. X., Sorensen, C. M., Ramer, E. R., Oliver, B. J., and Merklin, J. F., *Langmuir* 4:867-871 (1988).
  18. Gangopadhyay, S., Elminyawi, I., and Sorensen, C. M., *Appl. Opt.* 30:4859-4864 (1991).
  19. Charalampopoulos, T. T., and Chang, H., *Combust. Flame* 87:89-99 (1991).
  20. Sorensen, C. M., Cai, J., and Lu, N., submitted.
  21. Harris, S. J., *Combust. Sci. Technol.* 72:67-77 (1990).
  22. Garo, A., Prado, G., and Lahaye, J., *Combust. Flame* 79:226-233 (1990).
  23. Mulholland, G. W., Personal communication, 1991.

Received 30 March 1992; revised 18 September 1992

#### APPENDIX: THE MOMENT RATIOS $\bar{\kappa}$ AND $f_n$

The fractal power law relates the number of primary particles per aggregate to the ratio  $R_g/d_p$ :

$$n = k_f \left( \frac{R_g}{d_p} \right)^{D_f} \quad (\text{A1})$$

where  $D_f$  is the fractal dimension and  $k_f$  is the prefactor. The definition of the mean-square radius of gyration for a population of polydisperse aggregates consisting of monodisperse primary particles that is given by Eq. 6 is highly advantageous as discussed elsewhere [7]. The appropriate version of the power law expression that is applicable to a population of polydisperse aggregates is then found by solving Eq. A1 for  $R_g$ , substituting it into Eq. 6

and rearranging the result,

$$\bar{n}^{-1} = \bar{\kappa} \frac{R_g^2}{d_p^2} \quad (\text{A2})$$

where  $\bar{\kappa}$  is defined by

$$\bar{\kappa} = \frac{k_f^{2/D_f} \sum p(n) n \sum p(n) n^2}{\sum n^{2/D_f} n^2 p(n)} \quad (\text{A3})$$

When  $D_f = 2.0$ ,  $\bar{\kappa}$  is reduced to the quotient of  $k_f$  and a high moment ratio of the aggregate pdf:

$$\bar{\kappa} = k_f / \left( \frac{\bar{n}^3}{\bar{n}^2 \bar{n}^1} \right) \quad (\text{A4})$$

The polydispersion power law, Eq. A2, and thus also  $\bar{\kappa}$  enter into the expressions for the differential and total scattering cross sections when they are expressed in terms of the mean-square radius of gyration.

While there is now a well documented literature on the value of the  $D_f$  from both experimental observations and from computer simulations of cluster-cluster aggregation, very limited information exists on the value of  $k_f$ , and thus also on  $\bar{\kappa}$ . In a previous work [1] the value of  $k_f = 5.8$  that originates from a computer simulation [9] was employed. We now seek to determine an experimental value of  $k_f$  for use in determining  $\bar{\kappa}$ .

The first source of data on  $k_f$  is provided by the 36 aggregate subset sample of soot particles originating from an acetylene diffusion flame [16, 23]. These investigators reported  $n$  and  $R_g$  as determined from the two-dimensional projection, and also the maximum dimension of the aggregate  $L_{m_x}$ . From these data we find the average value of the ratio of  $L_{m_x}/R_g$  to be 3.55. Also from the tabular data of  $n$  and  $R_g$  listed in the same work, we directly find  $k_f = 9.22$  and  $D_f = 1.40$  by a regression analysis. The latter low value of  $D_f$  perhaps results from the small size of this subset sample. This body of data suggests a higher value of  $k_f$  for soot aggregates than was obtained from the computer simulation.

A second source of data on  $\bar{\kappa}$  is found using the above experimentally derived average value of  $L_{m,1}/R_c$  to convert the observed  $L_{m,1}$  [3] for the experimental data reported on the nonsmoking ethene flame. This leads to values of  $k_f = 8.9$  and  $8.3$  for the two aggregate populations that were analyzed. Based on all of above information, we adopt a value of  $k_f = 9.0$  as an experimentally based value that is specifically applicable to soot aggregates.

Values of  $\bar{\kappa}$  are found from its definition Eq. A3 using the detailed statistics of the latter two applicable population data sets. The resulting values are found to be  $\bar{\kappa} = 2.89$  and  $2.60$  corresponding to aggregate pdfs of intermediate width.

The moment ratio  $f_n$  given by Eq. 4 is more readily determined from the above sources of data to lie within the range of 1.6–1.8. This value is only somewhat smaller than the value applicable for the continuous self-preserving particle size distribution function for coagulating spherical droplets. Because  $f_n$  is defined in terms of low moments of the aggregate pdf, its value is more narrowly circumscribed and, accordingly, the value of  $f_n = 1.70$  is considered to be reliable for intermediate pdf widths.

The influence of the width of the aggregate population can be investigated by adopting a particular function for the pdf. The discrete log normal distribution is

$$p(n) = \frac{\exp \left[ - \left( \frac{\ln \frac{n}{n_c}}{3\sqrt{2} \sigma_g} \right)^2 \right]}{3\sqrt{2} \pi \sigma_g s_0 n} \quad (\text{A5})$$

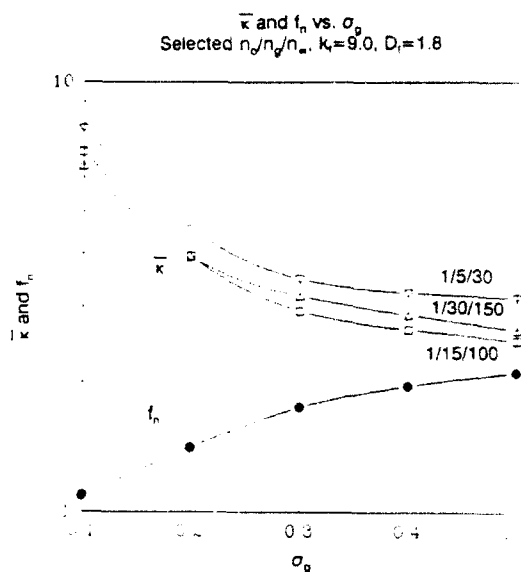


Fig. A1.  $\bar{\kappa}$  and  $f_n$  versus  $\sigma_g$  as calculated from a discrete log normal distribution for selected values of  $n_0/n_c/n_s$ .

where  $\sigma_g$  is the geometric standard deviation,  $n_c$  is the geometric mean number of primary particles per aggregate, and  $s_0$  is a constant defined such that  $p(n)$  summed over all sizes ( $n_0$  to  $n_c$ ) is unity. Values of  $f_n$  and  $\bar{\kappa}$  for log normal distributions can be found by inserting Eq. A5 into Eqs. 4 and A3 and evaluating the indicated summations for particular values of  $n_0$ ,  $n_c$ ,  $n_s$ ,  $\sigma_g$ ,  $D_f$ , and  $k_f$ . Some results are presented in Fig. A1 for  $D_f = 1.80$  and  $k_f = 9.0$ , and with  $n_0/n_c/n_s$  estimated to bracket the range of interest. For  $\sigma_g = 0.300$  corresponding to a moderate width of the pdf, the value of  $\bar{\kappa}$  ranges from 2.9 to 3.5 and  $f_n$  ranges from 1.63 to 1.75. Reasonable values of  $f_n$ ,  $\bar{\kappa}$  are 5.1 to 5.9 for aggregate populations of intermediate width.